Vectorial light–matter interactions: polarimetric parameters and applications



A Thesis Submitted to the Board of the Faculty of the Mathematical, Physical and Life Sciences Division for the degree of *Master of Science by Research* in the University of Oxford

Runchen Zhang

Wadham College

April 2026

Abstract

Vectorial light–matter interactions: polarimetric parameters and applications

By Runchen Zhang

The Mueller matrix provides a powerful and general foundation for describing polarization-related light–matter interactions by characterizing how optical systems and materials transform the state of polarization of light. However, the information encoded in a Mueller matrix is not directly transparent, and its full significance depends on how it is parameterized, physically interpreted, and ultimately translated into useful optical functionalities. To investigate this gap, this thesis studies the characterization of retarder properties in complex media and then extends the discussion towards the functional use and application of combined retarder–diattenuator systems.

First, the thesis examines the characterization of retarder properties in complex media. The results show that conventional decomposition-based parameters may lead to physically misleading interpretations when the internal structure of a retarder sample is unknown. To circumvent this, a set of elliptical retarder parameters is used to describe the retarder as a whole, without relying on restrictive structural assumptions. This approach is validated experimentally using layered and non-layered liquid crystal samples, demonstrating that it provides a

more physically plausible characterization of retarder properties in complex media.

The thesis then extends from pure retarder systems to systems containing both retarders and diattenuators. In this context, a retarder–diattenuator–retarder cascade framework is introduced for multiplexed vector beam conversion. An analytical design method is developed for the two-channel case, and a numerical design method for three-channel operation. The framework is demonstrated through the generation and conversion of Stokes skyrmion fields, showing that a single passive device can realize flexible and multiplexed polarization transformations. Further error analysis shows that the proposed framework supports high-precision polarization multiplexing up to three channels.

Taken together, these studies offer new insights into the role of the Mueller matrix as a foundation for understanding polarization-related light–matter interactions and supporting the design of polarization-based functionalities. A summary of the thesis and an outlook on future research are then provided, focusing on the joint interpretation of multiple polarimetric properties and their integration with non-polarimetric information for more advanced analysis and applications.

Acknowledgements

My time at Oxford has been shaped by the support, guidance, and generosity of many people, to whom I am deeply grateful. First and foremost, I would like to express my sincere thanks to Prof. Stephen Morris and Prof. Steve Elston for offering me the opportunity to come to Oxford and for supporting me throughout this journey. Your guidance, encouragement, and high standards have shaped both my work and my way of thinking. I have always admired your leadership, your breadth of vision, and your generosity in supporting younger researchers, and I feel very fortunate to have learned from you and be part of the Soft Matter Photonics group. I would like to express my deepest gratitude to Prof. Chao He. Your influence on my life has extended far beyond research supervision. You have guided me not only in academic work, but also in how to think, how to make decisions, and how to face life with resilience and clarity. Under your supervision, I received invaluable guidance in research and learned how to think more clearly and work more rigorously. It has been a privilege to be part of the Vectorial Optics and Photonics group and I truly believe that there are many meaningful achievements still ahead of us.

I am grateful to Prof. Martin Booth for his advice and support on my work. I am likewise grateful to Prof. Patrick Salter for his support, insight, and valuable advice, which I have greatly appreciated. I have long admired your work and

learned a great deal from it. My sincere thanks also go to Dr. Jingyu Wang for patient guidance and generous help.

I would like to thank my colleagues and friends, who made these years not only productive but also deeply memorable. In particular, Dr. Yifei Ma, thank you for your constant and invaluable help. I have learned a great deal from you, not only in research but also in how to understand people and navigate the wider world. Dr Xuke Qiu, thank you for the many helpful discussions and for so generously sharing your experience and insights. Dr Zhikai Pong, I am grateful for your support as a colleague and collaborator. Mr Yunqi Zhang, your steady support and kindness throughout this time have meant a great deal to me. Mr Jinge Guo and Zhiyu Xu, thank you for your friendship, your support, and the many enjoyable conversations we shared. I am also grateful to Xiaoyi Shang, Ruofu Liu, Zimo Zhao, Linquan Yuan, Tade Marozsak, Zhenglin Li, and others for your kindness, patience, and the many thoughtful conversations from which I learned so much.

Finally, I would like to thank my parents. Your love and support have been the foundation beneath everything. I have always felt fortunate to have your love, trust, and understanding throughout my life. Thank you for your guidance, for your patience, and for supporting me in every decision I have made. No matter

where life takes me, home will always remain the safest and most enduring harbour in my heart. With all my love and gratitude.

Runchen Zhang

April 2026

Publication

Publications forming part of this thesis:

1. **Runchen Zhang**, Xuke Qiu, Yifei Ma, Zimo Zhao, An Aloysius Wang, Jinge Guo, Ji Qin, Steve J. Elston, Stephen M. Morris, and Chao He. **Elliptical vectorial metrics for physically plausible polarization information analysis**. *Advanced Photonics Nexus* **4(6)**, 066015 (2025).

2. [**Runchen Zhang**, Tade Marozsak, An Aloysius Wang, Yunqi Zhang], Yifei Ma, Tingxian Gao, Haochuan Geng, Qihao Han, Ben Dai, Steve J. Elston, Stephen M. Morris, and Chao He. **Multiplexed vector beam conversion via complex structured matter**. arXiv preprint arXiv:2512.22980 (2025). *Co-first author (equal contribution)*

Other publications related to this work:

3. [Yunqi Zhang, An Aloysius Wang, **Runchen Zhang**], Zimo Zhao, Yifei Ma, Ruofu Liu, Zhi-Kai Pong, Yuxi Cai, and Chao He. **Skyrmions based on optical anisotropy for topological encoding**. arXiv:2508.16483 (2025). Accepted by *Light Sci Appl*. *Co-first author (equal contribution)*

4. Xuke Qiu, **Runchen Zhang**, Yifei Ma, Zimo Zhao, Zipei Song, Alva C. J. Orr, Mengmeng Li, Waqas Kamal, Jinge Guo, Alfonso A. Castrejón-Pita, Steve J. Elston, Stephen M. Morris, and Chao He. **Complex structured light**

generation using printed liquid crystal droplets. *Advanced Optical Materials* **13**, e02276 (2025).

5. An Aloysius Wang, Zimo Zhao, Yifei Ma, Yuxi Cai, **Runchen Zhang**, Xiaoyi Shang, Yunqi Zhang, Ji Qin, Zhi-Kai Pong, Tádé Marozsák, Binguo Chen, Honghui He, Lin Luo, Martin J Booth, Steve J Elston, Stephen M Morris, Chao He. **Topological protection of optical skyrmions through complex media.** *Light Sci Appl* **13**, 314 (2024). *Elected as Annual Back Cover*

Conference

SPIE Photonics West 2026 – Poster presentation

Title: A set of alternative parameters for polarization information analysis in a physically plausible way

San Francisco, US, January 2026

Photonics and Electromagnetics Research Symposium 2025 – Oral presentation

Title: A multiplexed vector beam converter for structured polarization manipulation

Chiba, Japan, November 2025

The Oxford International Conference on Advanced Optics and Photonics (highlighted by UNESCO's International Day of Light) – Oral presentation (Outstanding Presentation Award)

Title: An alternative set of vectorial metrics for information analysis

Oxford, UK, July 2024

British Liquid Crystal Society Annual Meeting 2024 – Poster presentation

Title: An alternative set of vectorial metrics for information analysis

Oxford, UK, April 2024

List of Abbreviations

SoP	State of polarization
PSA	Polarization state analyzer
PSG	Polarization state generator
PS	Poincaré sphere
SkyN	Skyrmion number
LC	Liquid crystal
MMPD	Mueller matrix polar decomposition
CR	Circular retarder
LR	Linear retarder
ER	Elliptical retarder
MMT	Mueller matrix transformation

Content

Chapter 1 Overview 13

1.1 Introduction 13

1.2 Research motivation 14

1.3 Thesis outline 17

Chapter 2 Background 19

2.1 Foundation of polarization optics 19

2.1.1 Theoretical frameworks 20

2.1.1.1 Jones calculus 21

2.1.1.2 Stokes–Mueller Formalism 22

2.1.2 Non-depolarizing polarization elements 24

2.1.2.1 Retarder 25

2.1.2.2 Diattenuator 26

2.2 Polarimetric measurement and analysis 27

2.2.1 Polarimetry 27

2.2.2 Polarimetric parameter extraction 30

2.2.2.1 Direct measurements 31

2.2.2.2 Model-based parameter extraction 32

2.2.2.3 Data-driven feature extraction 34

2.3 Roles of polarization in optical measurement and beam modulation 35

2.3.1 Mueller matrix polarimetry for biomedical applications 36

2.3.1.1 Transmissive geometry for thin tissue assessment 36

2.3.1.2 Backscattering geometry for bulk tissue assessment 37

2.3.2 Polarization modulation for structured light 38

2.4 Summary 38

Chapter 3 Polarization information analysis in complex media 40

3.1 Concept 40

3.1.1 Conventional decomposition 41

3.1.2 ER metrics for physically plausible analysis 42

3.2 Experimental validation 44

3.2.1 Experimental details 45

3.2.1.1 LC sample fabrication 45

3.2.1.2 Data collection 47

3.2.2 Limitations of layer-based decomposition model 50

3.2.2.1 Stacked linear–circular retarder sample 50

3.2.2.2 Stacked-linear-retarder sample 52

3.2.2.3 Non-layered LC droplet sample 54

3.2.3 Elliptical retarder-based characterization 56

3.3 Discussion and summary 59

Chapter 4 Simulation-based demonstration of multiplexed vector beam conversion using combined retarders and a diattenuator 62

4.1 Concept 62

4.1.1 Conventional methods for polarization modulation 63

4.1.2 Cascade framework for multiplexed polarization conversion 64

4.1.3 Implementation of the framework 68

4.1.3.1 Analytical method 68

4.1.3.2 Numerical method 70

4.2 Framework demonstration via Stokes skyrmion multiplexing 72

4.2.1 Three-channel skyrmion generation 73

4.2.2 Three-channel skyrmion converter 75
4.2.3 Error analysis and multiplexing capacity 77
4.3 Discussion and summary 80
Chapter 5 Conclusion and future work 86
5.1 Conclusion 86
5.2 Future work 88
5.2.1 Joint interpretation of polarimetric parameters 89
5.2.2 Fusion of polarimetric and non-polarimetric information 90
References 94

Chapter 1 Overview

1.1 Introduction

This thesis investigates the analysis and applications of polarimetric parameters in light–matter interactions from a Mueller matrix perspective. Polarization provides a powerful way to analyze light–matter interactions and to support optical design. In this context, the Mueller matrix offers a general description of how optical systems and materials transform the state of polarization (SoP) of light.

From this Mueller matrix viewpoint, the thesis takes the vectorial information of matter as its starting point. In particular, the polarimetric parameters derived from the Mueller matrix are used to describe how optical systems and materials modify the SoP of light through their material structure. This makes them useful not only as measurable quantities, but also as a way to analyze the underlying polarization properties of matter itself. On this basis, the thesis explores how Mueller-matrix analysis can be developed from the fundamental description of complex media towards broader polarization-based applications.

The thesis develops this perspective in two stages. It begins with retarder-related properties and examines how retarder information should be described when the

internal structure of a sample is unknown. It then extends the discussion to systems containing both retarders and diattenuators, where polarimetric parameters are further used for the design and potential application of functional polarization transformations. Together, these studies establish a coherent progression from single to combined polarimetric properties on a Mueller-matrix foundation.

1.2 Research motivation

Polarization is a fundamental degree of freedom of light. When light interacts with a material or optical system, the SoP of the incident light is modified by the polarization properties of the object[1]. These properties are an essential part of modern optical measurement and modulation, making the description of polarization-related light–matter interactions a central task in polarization optics[2]. Among the available theories, the Mueller matrix provides one of the most general descriptions of this process[3]. It has been widely applied in biomedical imaging[4], material characterization[5], and structured-light optics[6]. However, the Mueller matrix itself is only a mathematical representation. It does not directly reveal the underlying physical properties of a sample or device, and further analysis is required to translate Mueller-matrix-derived information into meaningful physical parameters or useful optical functionalities[1,3].

To address this, a wide range of methods have been proposed in both characterization and modulation. For characterization, various approaches have been developed to derive physically interpretable parameters from Mueller matrices, such as polar decomposition[7], differential decomposition[8], symmetric decomposition[9], transformation-based method[10] and more recent data-driven methods[11]. For modulation, a variety of platforms have also been introduced, such as q-plate[12], metasurface[13,14], gradient-index lens[15,16], glass cone[17], and waveplate array[18,19]. Overall, these developments have greatly expanded the analytical and functional scope of polarization optics.

Despite this progress, important limitations remain. In characterization, the physical meaning of derived parameters often depends strongly on the chosen parameterization, and such descriptions are not always unique or reasonable, especially when the internal structure of the sample is unknown[7]. In modulation, many existing approaches are closely tied to restricted classes of transformations, which limits their ability to support multiple functionalities[20].

Taken together, these points suggest that, although the Mueller matrix is already a powerful foundation for describing polarization-related light–matter interactions, its potential has not yet been fully realized[21].

Accordingly, the present thesis is motivated by two main directions:

(1) **Physically meaningful characterization of retarder properties:** Retarder information is of particular interest in many applications. However, conventional descriptions often rely on restrictive structural assumptions and may therefore lead to physically misleading interpretations when the internal structure of a sample is unknown. This motivates the first part of the thesis, which investigates how retarder properties can be described in a more physically plausible way in complex media.

(2) **Multiplexed functional use of multiple polarimetric properties:** Existing passive approaches to polarization modulation are often based mainly on retarders. This motivates a broader perspective in which additional polarimetric properties, particularly diattenuation, are incorporated together with retardance into a more general framework for polarization transformation. The second part of the thesis therefore explores how combined retarder–diattenuator systems can be used to realize multiplexed polarization transformations.

These two directions show how the Mueller matrix can serve not only as a foundation for describing polarization-related light–matter interactions, but also as a basis for interpreting and engineering them in a more advanced way.

1.3 Thesis outline

Chapter 2 provides the theoretical background for the thesis. It begins with the fundamental description of polarization using Jones calculus and the Stokes–Mueller formalism. It then introduces the two non-depolarizing polarization elements that are central to this thesis, namely retarders and diattenuators. The chapter further reviews polarimetric measurement and parameter extraction, ranging from directly measured quantities to model-based and data-driven parameters. Finally, it outlines two main application directions of polarization, namely Mueller polarimetry for biomedical characterization and polarization modulation for structured light. This chapter provides the necessary context for understanding the research presented in the subsequent chapters.

Chapter 3 focuses on polarization information analysis in complex media. It examines how retarder-related properties should be described when the internal structure of a sample is unknown. After discussing the limitations of conventional layer-based decomposition, the chapter introduces a set of elliptical retarder (ER) parameters as a more physically plausible description of unknown retarder systems. Experimental studies on layered and non-layered liquid crystal (LC) samples are then presented to validate this approach. This chapter establishes a more suitable framework for characterizing retarder properties in samples with

unknown structure. The research presented in this chapter formed the basis of the publication *Advanced Photonics Nexus* **4**(6), 066015 (2025).

Chapter 4 extends the discussion from pure retarder systems to optical systems containing both retarders and diattenuators. It introduces a cascade framework for multiplexed polarization conversion and presents both analytical and numerical implementation methods for its design. The proposed framework is then demonstrated through the generation and conversion of Stokes skyrmions, together with an analysis of its multiplexing capacity. This chapter shows how combined retarder–diattenuator systems can be used for functional polarization transformation and device design. The research presented in this chapter formed the basis of the preprint "Multiplexed vector beam conversion via complex structured matter", arXiv: 2512.22980 (2025), which is currently under major revision at *Nature Communications*.

Chapter 5 concludes the thesis and outlines possible future directions. It first summarizes the main progression of the thesis. Then, it discusses two possible directions for future work: the joint interpretation of multiple polarimetric parameters, and the fusion of polarimetric and non-polarimetric information for more advanced analysis and applications.

Chapter 2 Background

2.1 Foundation of polarization optics

For a monochromatic electromagnetic wave propagating in a homogeneous medium, the electric field can be expressed as

$$\mathbf{E}(\mathbf{r},t) = \Re\left\{\mathbf{E}_0 e^{i(\mathbf{k}\cdot\mathbf{r}-\omega t)}\right\}, \tag{2.1}$$

where $\mathbf{E}_0$ is the complex amplitude vector, $\mathbf{k}$ is the wave vector, and ω is the angular frequency[22]. For a plane wave propagating along the z-direction, the electric field is transverse to the direction of propagation, and can therefore be written in terms of two orthogonal components in the x and y directions as

$$\mathbf{E}(z,t) = \Re\left\{\left(E_x\hat{\mathbf{x}}+E_y\hat{\mathbf{y}}\right)e^{i(kz-\omega t)}\right\}, \tag{2.2}$$

where E_x and E_y are complex quantities describing the amplitudes and phases of the electric-field components along the x- and y- axes, respectively.

For fully polarized light, these components can be written as

$$E_x = E_{0x}e^{i\delta_x}, E_y = E_{0y}e^{i\delta_y}, \tag{2.3}$$

where E_{0x} and E_{0y} denote the real-valued amplitudes, and δ_x and δ_y represent the corresponding phases. The relative amplitudes and phase difference $\delta_x - \delta_y$ together determine the state of polarization (SoP) of the light.

Based on this representation of the electric field, the SoP of light and its evolution through optical systems can be described using two widely adopted mathematical frameworks: Jones calculus and the Stokes–Mueller formalism. The former is applicable to fully polarized light and non-depolarizing media, whereas the latter offers a more general description that can additionally account for partial polarization and depolarization effects. Combined, these formalisms provide the theoretical basis for analysing polarization phenomena in optical systems. In this thesis, only relative phase differences between polarization components are considered, and the absolute phase of the electric field is not treated, as it does not affect the polarization state.

2.1.1 Theoretical frameworks

To quantitatively describe polarization states and their evolution in optical systems, two complementary theoretical frameworks are introduced in the following sections: Jones calculus and the Stokes–Mueller formalism. These frameworks provide different but consistent descriptions of polarization and together form the basis for the analysis methods used throughout this thesis.

In this context, several scope limitations are specified. First, the analysis focuses on the SoP of light rather than its absolute intensity. Second, only relative phase differences between orthogonal field components are considered, as the absolute

phase of the electromagnetic field does not affect the polarization state. Finally, the discussion is restricted to deterministic polarization transformations under linear optical systems

2.1.1.1 Jones calculus

For fully polarized light, the two orthogonal electric-field components can be conveniently written in vector form. This provides a compact representation of the polarization state and serves as the starting point of Jones calculus[1,23]. Specifically, these two components can be arranged into a 2×1 vector

$$E = \begin{pmatrix} E_x \\ E_y \end{pmatrix} = \begin{pmatrix} E_{0x} e^{i\delta_x} \\ E_{0y} e^{i\delta_y} \end{pmatrix}, \tag{2.4}$$

which is known as the Jones vector. It can represent the physical properties of any fully polarized light field. Subsequently, when fully polarized light propagates through a medium, its polarization state is modified, resulting in a new vector E'. Assuming a linear relationship between input and output fields, this transformation can be written as

$$\begin{pmatrix} E'_x \\ E'_y \end{pmatrix} = \begin{pmatrix} J_{xx} & J_{xy} \\ J_{yx} & J_{yy} \end{pmatrix} \begin{pmatrix} E_x \\ E_y \end{pmatrix}, \tag{2.5}$$

or

$$E' = JE, \tag{2.6}$$

where

$$J = \begin{pmatrix} J_{xx} & J_{xy} \\ J_{yx} & J_{yy} \end{pmatrix}. \tag{2.7}$$

This 2×2 matrix in Eq. (2.7) is called the Jones matrix, which represents the polarization properties of the medium. The Jones vector and Jones matrix together form the basis of Jones calculus.

A drawback of Jones calculus is that it is limited to fully polarized light and cannot describe depolarization effects. To address this limitation, the Stokes–Mueller formalism is employed, which provides a more general framework for describing polarization.

2.1.1.2 Stokes–Mueller Formalism

In this formalism, the polarization state is represented by a 4×1 Stokes vector[24,25]

$$\boldsymbol{S} = \begin{pmatrix} S_0 \\ S_1 \\ S_2 \\ S_3 \end{pmatrix} = \begin{pmatrix} E_{0x}^2 + E_{0y}^2 \\ E_{0x}^2 - E_{0y}^2 \\ 2E_{0x}E_{0y}\cos\delta \\ 2E_{0x}E_{0y}\sin\delta \end{pmatrix} = \begin{pmatrix} I \\ I_x - I_y \\ I_{45^\circ} - I_{-45^\circ} \\ I_R - I_L \end{pmatrix} \tag{2.8}$$

Here, the Stokes parameters have clear physical interpretations: S_0 represents the total intensity of light, S_1 represents the amount of linear horizontal or vertical polarization, S_2 represents the amount of linear $+45^\circ$ or -45° polarization, and S_3 represents the amount of right or left circular polarization contained within the beam. From the above definition, the following inequality holds:

$$S_0^2 \geq S_1^2 + S_2^2 + S_3^2, \tag{2.9}$$

where equality corresponds to fully polarized light. As shown below, **Table 2.1** summarizes the normalized Jones and Stokes vectors for several fundamental polarization states.

Polarization state	Horizontal linear	Vertical linear	$+45°$ linear	$-45°$ linear	Right circular	Left circular
Jones vector	$\begin{pmatrix}1\\0\end{pmatrix}$	$\begin{pmatrix}0\\1\end{pmatrix}$	$\frac{1}{\sqrt{2}}\begin{pmatrix}1\\1\end{pmatrix}$	$\frac{1}{\sqrt{2}}\begin{pmatrix}1\\-1\end{pmatrix}$	$\frac{1}{\sqrt{2}}\begin{pmatrix}1\\i\end{pmatrix}$	$\frac{1}{\sqrt{2}}\begin{pmatrix}1\\-i\end{pmatrix}$
Stokes vector	$\begin{pmatrix}1\\1\\0\\0\end{pmatrix}$	$\begin{pmatrix}1\\-1\\0\\0\end{pmatrix}$	$\begin{pmatrix}1\\0\\1\\0\end{pmatrix}$	$\begin{pmatrix}1\\0\\-1\\0\end{pmatrix}$	$\begin{pmatrix}1\\0\\0\\1\end{pmatrix}$	$\begin{pmatrix}1\\0\\0\\-1\end{pmatrix}$

Table 2.1. Normalized Jones and Stokes vectors representing common polarization states, including linear (horizontal, vertical, $+45°$, $-45°$) and circular (right-handed, left-handed) polarized light.

Analogous to the Jones formalism, the transformation of the Stokes vector through a medium can be described by a linear operation:

$$S' = MS, \tag{2.10}$$

where M is a 4×4 Mueller matrix[1,23]

$$M = \begin{pmatrix} m_{00} & m_{01} & m_{02} & m_{03} \\ m_{10} & m_{11} & m_{12} & m_{13} \\ m_{20} & m_{21} & m_{22} & m_{23} \\ m_{30} & m_{31} & m_{32} & m_{33} \end{pmatrix}. \quad (2.11)$$

Each element m_{ij} describes how the j-th component of the input Stokes vector contributes to the i-th component of the output Stokes vector. The Mueller matrix therefore provides a complete description of the polarization properties of a medium[26–30], including depolarization effects. Unlike Jones calculus, which requires both amplitude and phase information, the Stokes–Mueller formalism relies solely on intensity measurements. Since intensity can be directly recorded using detectors such as CCD cameras, this formalism is more practical for experimental implementations. Consequently, most modern polarization microscopy techniques are based on measuring either the Stokes vector or the Mueller matrix[26,28–30].

2.1.2 Non-depolarizing polarization elements

To relate the mathematical formalisms introduced above to physically realizable systems, it is necessary to consider the fundamental types of polarization elements. In general, polarization optics involves a variety of optical components, including retarders, diattenuators and depolarizers. These elements describe how the SoP of light is modified upon propagation through structured materials or optical devices.

In this thesis, the discussion is restricted to non-depolarizing optical elements. In such systems, fully polarized light remains fully polarized after interaction, and the transformation can be fully described by Jones matrices or, equivalently, by non-depolarizing Mueller matrices. Depolarizing effects, which arise from incoherent processes such as multiple scattering or spatial averaging, are not considered in this work.

Two fundamental polarization elements are of primary interest in this work: retarders and diattenuators. Retarders, such as linear and circular waveplates, modify the polarization state by introducing phase differences between orthogonal components of light without altering the total intensity. Diattenuators, such as linear and circular polarizers, introduce polarization-dependent attenuation and selectively transmit specific polarization states. These two elements form the basic building blocks for describing and engineering polarization transformations in non-depolarizing optical systems.

2.1.2.1 Retarder

A retarder is a non-depolarizing optical element that modifies the SoP of light by introducing a phase delay between two orthogonal polarization components[1]. This phase delay, referred to as the retardance, arises because the two components experience different refractive indices and therefore propagate at different speeds

along the two principal axes of the material. Among these axes, the one along which light accumulates the smaller phase shift is known as the fast axis, while the orthogonal one is referred to as the slow axis.

In polarization optics, retarders preserve the intensity of the incident light and can be represented by $SU(2)$ matrices in the Jones formalism or equivalently by $SO(3)$ matrices in Mueller calculus[3]. On the Poincaré sphere (PS), their action corresponds to a three-dimensional rotation, where the orientation of the fast axis defines the rotation axis and the retardance determines the rotation angle. The Mueller matrix of a retarder can be written as

$$M_R = \begin{pmatrix} 1 & 0 \\ 0 & m_R \end{pmatrix} \tag{2.12}$$

where m_R is a 3×3 rotation matrix. Given the retardance and the orientation of the fast axis, m_R can be constructed using Rodrigues' rotation formula[1,31].

2.1.2.2 Diattenuator

A diattenuator is an optical element that introduces polarization-dependent attenuation, such that different polarization components are transmitted with different efficiencies[1]. On the PS, its action can be interpreted as a contraction of the Stokes vector towards a preferred axis. A horizontal linear diattenuator can be characterized by its amplitude transmission coefficients p_x and p_y along the horizontal and vertical principal axes, respectively. When polarized light passes

through such an element, the horizontal polarization component is attenuated by a factor of p_x, while the vertical component is attenuated by a factor of p_y. The transmission ratio p is defined as

$$p = \frac{p_y}{p_x} \tag{2.13}$$

and the corresponding Mueller matrix of a horizontal linear diattenuator (M_D) is given by

$$M_D = \frac{1}{2}\begin{pmatrix} 1+p^2 & 1-p^2 & 0 & 0 \\ 1-p^2 & 1+p^2 & 0 & 0 \\ 0 & 0 & 2p & 0 \\ 0 & 0 & 0 & 2p \end{pmatrix}. \tag{2.14}$$

2.2 Polarimetric measurement and analysis

Building on the theoretical frameworks and polarization elements introduced in the previous section, this section focuses on the practical measurement and quantitative analysis of polarization. In particular, polarimetric techniques for measuring the Mueller matrix of a sample are first introduced. Subsequently, methods for extracting physically meaningful parameters from polarimetric data are discussed. These parameters provide quantitative descriptors of polarization properties and form the basis for further analysis and applications throughout this thesis.

2.2.1 Polarimetry

Polarimetry is a widely used technique for measuring the SoP of light and how this state is modified after interaction with an object or medium. It encompasses

a broad range of techniques, from partial measurements of selected polarization properties to full characterization of the polarization state or the sample. In this thesis, the focus is placed on full-Mueller matrix polarimetry. Partial polarimetric methods, which measure only a subset of polarization parameters, are also acknowledged as important in applications requiring higher measurement speed or reduced system complexity[32–38].

Polarimetry can be understood in terms of two fundamental modules: the polarization state generator (PSG) and the polarization state analyzer (PSA)[39]. The PSG prepares incident light in a set of known polarization states, while the PSA analyses the outgoing light by projecting it onto different polarization bases. When only the PSA is employed, the Stokes vector of the light can be measured. When both PSG and PSA are used in combination, the full Mueller matrix of the sample can be reconstructed. This PSG–PSA framework provides a unified description of most polarimetric measurement systems.

In early implementations, the PSG and PSA were usually constructed from combinations of rotating waveplates and/or polarizers[39–41]. During measurement, the rotation of these optical elements changes the polarization states generated and analyzed, enabling reconstruction of the sample Mueller matrix. Although such systems are relatively straightforward to implement, their development has been

limited by low imaging speed and reduced precision arising from mechanical constraints.

To overcome these limitations, a range of faster polarization modulation methods has been introduced, including liquid crystal (LC) variable retarders[42], spatial light modulators[43], and photoelastic modulators[44]. A schematic of a LC-based Mueller matrix polarimetry system is shown in the **Figure 2.1**. The system consists of a PSG and a PSA arranged on either side of the sample. The PSG, composed of a linear polarizer P_1 and two LC variable retarders (R_1, R_2), generates a set of incident polarization states by electrically tuning the retardance of the LC elements. After interacting with the sample, the transmitted light is analyzed by the PSA, which consists of two additional LC variable retarders (R_3, R_4) and a linear polarizer P_2. By sequentially varying the retardances of the LC retarders in both the PSG and PSA, a series of intensity measurements is acquired by the CCD. These measurements are then used to reconstruct the Mueller matrix of the sample, enabling a fast and complete characterization of its polarization properties.

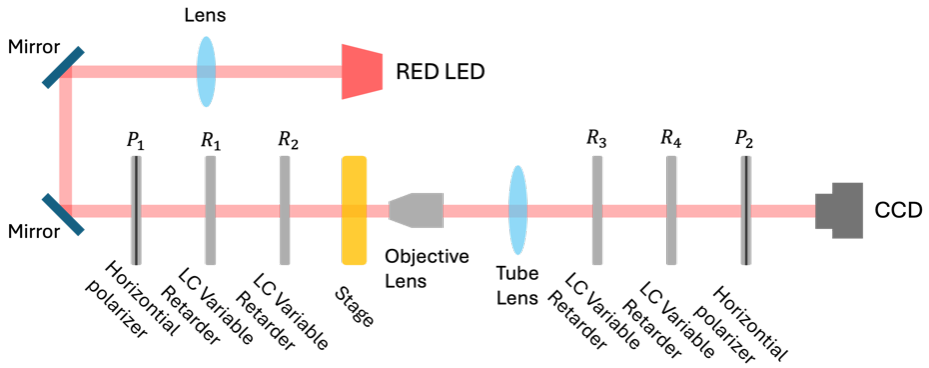


Figure 2.1. Schematic of a Mueller matrix polarimeter based on LC variable retarders. P_1 and P_2 represent horizontal linear polarizers, while R_1 – R_4 represent LC variable retarders. Together, P_1, R_1, and R_2 constitute the PSG, which produces incident light with different polarization states, whereas R_3, R_4, and P_2 constitute the PSA, which analyzes the SoP of the light after interaction with the sample.

2.2.2 Polarimetric parameter extraction

Polarimetric data can be analyzed at different levels to characterize the polarization properties of a sample. In this thesis, the corresponding analysis approaches are grouped into three categories: direct measurements, model-based parameter extraction, and data-driven feature extraction[4,11,45]. Direct measurements are obtained directly from experimental observations. Model-based parameter extraction uses mathematical models or decomposition methods to derive physically meaningful parameters from polarimetric data. Data-driven feature extraction further processes these measurements or derived parameters to obtain higher-level descriptors, such as texture, contrast, or AI-derived features.

2.2.2.1 Direct measurements

Direct measurements refer to polarization-related quantities obtained directly from experimental observations. In polarization imaging, such quantities provide straightforward and often practically useful contrast associated with specific sample polarization properties[11,46]. For example, Jacques *et al.* used polarizers oriented parallel and perpendicular to the incident polarization at the detection side to acquire two intensity images, I_{par} and I_{per}, respectively. Based on these measurements, they defined the parameter $I_{\mathrm{pol}} = \frac{I_{\mathrm{par}} - I_{\mathrm{per}}}{I_{\mathrm{par}} + I_{\mathrm{per}}}$, which was shown to enhance edge contrast in skin cancer images. Oldenbourg *et al.* developed a polarized light microscope capable of directly measuring the retardance and slow-axis orientation of small birefringent samples[47,48]. Antonelli reported that the m_{22} and m_{33} elements of the Mueller matrix can be used to distinguish colon cancer tissue, as their absolute values are larger in diseased regions[49]. Pierangelo further used the m_{22} element as an indicator of the depolarizing ability of the sample[50].

However, such quantities provide only limited polarization information about the sample. For more comprehensive characterization, Mueller matrix polarimetry has become the mainstream approach. Since the Mueller matrix is itself a mathematical representation, further processing is needed to derive physically meaningful parameters, as discussed in the following section.

2.2.2.2 Model-based parameter extraction

Model-based parameter extraction aims to derive physically meaningful quantities from polarimetric data through mathematical models, decomposition methods, or transformation-based analysis[11,45]. Among these approaches, Mueller matrix polar decomposition (MMPD) is one of the most widely used methods[7]. In this framework, the Mueller matrix is decomposed into the product of diattenuator, retarder, and depolarizer submatrices, from which the corresponding physical parameters can be extracted:

$$M = M_{\Delta} M_R M_D. \tag{2.15}$$

The diattenuator is characterized by the diattenuation D and its axis[51]. The retarder is often further decomposed into a circular retarder (CR) and a linear retarder (LR)[52,53], and is then described by the linear retardance δ, linear axis orientation θ, and circular retardance ϕ. The depolarizer is characterized by the depolarization Δ and the degree of polarizance P. It describes the change in the degree of polarization of the incident light. These MMPD-derived parameters correspond to specific polarization properties of the sample and can be obtained through operations on the Mueller matrix[54].

To avoid the ordering ambiguity associated with the non-commutative nature of matrix multiplication in MMPD, Ortega-Quijano *et al.* proposed the Mueller matrix differential decomposition method[8]. The resulting differential parameters

can provide a comprehensive description of the anisotropic and depolarizing properties of the medium. Ossikovski further verified the validity and applicable conditions of the differential matrix formalism[55]. In addition, by symmetrically decomposing the Mueller matrix, Ossikovski proposed the Mueller matrix symmetric decomposition, which is mathematically simpler than MMPD[9]. Zeng *et al.* developed the rotating linear polarization imaging technique and obtained the parameters by fitting sinusoidal curves[56,57].

Inspired by both MMPD and rotating linear polarization imaging technique, He *et al.* proposed the Mueller matrix transformation (MMT) method by fitting Monte Carlo simulation and experimental results with trigonometric curves[10]. In this method, the parameter A is closely related to the anisotropy of the medium, x is associated with the alignment of fibrous structures, and b is related to scatterer size. Building on this idea, additional parameters have been proposed by analyzing the behaviour of the Mueller matrix under different transformations. For example, Gil introduced a set of invariant parameters that remain unchanged under rotation and retarder transformations[58]. Li *et al.* further proposed additional parameters based on the symmetries of rotation and mirror transformations[59,60].

Together, these approaches provide physically interpretable parameter representations of polarimetric data. Based on these representations, more

advanced data-driven feature extraction methods have recently attracted increasing attention, particularly in combination with machine learning techniques.

2.2.2.3 Data-driven feature extraction

Data-driven feature extraction aims to identify higher-level parameters from polarimetric measurements or model-derived parameters, with the goal of capturing biologically or pathologically relevant image information. In this context, statistical, textural, and machine-learning-based methods have been increasingly used to reveal patterns that are not directly accessible from individual physical parameters alone[11,45,61,62].

For example, Dong *et al.* showed that texture features extracted from MMPD and MMT images can serve as quantitative indicators for detecting breast ductal carcinoma tissues at different stages[63]. Liu *et al.* applied the Tamura image processing method to MMPD and MMT parameter images to distinguish Crohn's disease in inflammatory bowel disease[64]. Zhai *et al.* further demonstrated that texture features extracted from polarization staining images can be used for tissue differentiation[65]. Similarly, Hou *et al.* showed that data-driven polarimetric features can accurately discriminate between high-grade squamous intraepithelial lesions and cervical squamous cell carcinoma[66]. In ophthalmology, Xi *et al.* used

model-derived polarimetric parameters as inputs to support vector machine classifiers and achieved high accuracy in distinguishing different scar tissue types associated with glaucoma surgery[67]. In addition, several machine-learning-based frameworks have been developed using polarimetric measurements or derived parameters[68–71].

Overall, the combination of polarization imaging with data-driven analysis, particularly machine learning and large-scale data processing, represents a promising direction for future development.

2.3 Roles of polarization in optical measurement and beam modulation

Polarization is a useful degree of freedom for optical measurement and structured light modulation. In optical measurement, changes in the polarization state induced by a sample can be used to infer its structural properties. In structured light modulation, the polarization response of a device can be engineered to transform incident fields into desired output fields with tailored polarization distributions for specific functionalities. The following sections briefly introduce these two different use cases.

2.3.1 Mueller matrix polarimetry for biomedical applications

In biomedical applications, Mueller matrix polarimetry provides a powerful foundation for relating sample-induced polarization changes to the underlying biological and pathological characteristics[4]. In particular, birefringence associated with fibrosis has attracted considerable attention[4,72]. By measuring sample birefringence, Mueller matrix polarimetry can reveal the distribution and density of collagen fibres. Since fibrosis changes significantly during cancer development, its quantitative assessment has become an important application of Mueller matrix polarimetry. The following sections discuss these biomedical applications in two major measurement geometries.

2.3.1.1 Transmissive geometry for thin tissue assessment

Transmissive polarization microscopy is one of the most widely used approaches in biomedical applications. Since transmissive polarization microscopy requires sufficient transmission of polarized light through the sample, it is primarily applied to the pathological examination of *ex vivo* thin tissue sections. These sections are typically prepared from fibrous regions or from areas where the degree of fibrosis changes markedly during disease progression. Over the past decades, this technique has contributed to the diagnosis of a wide range of cancers, including breast cancer[45,63,73,74], colon cancer[50,75–78], cervical cancer[79–82], skin

cancer[83–85], liver cancer[86,87], giant cell tumour of bone[71], and gastrointestinal cancer[88].

2.3.1.2 Backscattering geometry for bulk tissue assessment

In contrast to transmissive configurations, backscattering polarization microscopy is more suitable for *ex vivo* or *in vivo* bulk tissues, where a substantial fraction of the incident light is reflected. In studies of *ex vivo* bulk tissue, the main focus remains on fibrosis-related features. For example, fibrous structures in tissues such as tendons[89], skin[90], bladder[91], and myocardial muscle[92] can be identified through their linear birefringence properties. In addition, the depolarization properties of bulk tissue can also provide valuable structural information[93–95].

For *in vivo* applications, the emphasis shifts from tissue characterization to direct clinical use. Polarization endoscopy, as a minimally invasive technique, can provide valuable intraoperative diagnostic information. It has been applied in rat abdomens[33] and porcine bladders[91], revealing their polarization characteristics. More recently, it has also been used for the diagnosis of cancerous lesions, demonstrating that real-time polarization information can assist clinical cancer diagnosis[96]. In addition, Mueller matrix colposcopy has shown considerable potential for supporting the clinical diagnosis of cervical cancer[97,98].

2.3.2 Polarization modulation for structured light

Polarization modulation focuses on tailoring the SoP of light to achieve specific optical functionalities[6]. By designing optical elements or structured media with controlled polarization responses, it is possible to manipulate the amplitude, phase and polarization distribution of light in a coordinated manner. This capability plays a central role in modern photonics, enabling applications such as beam shaping, information encoding, and optical signal processing.

From the implementation perspective, polarization modulation for structured light can be realized using structured matter with spatially varying polarization responses. Such media can apply different polarization transformations at different transverse positions of the beam, allowing the amplitude, phase, and polarization state of the output field to be shaped in a coordinated manner. Such control has been widely explored in areas such as vector beam generation, polarization multiplexing, and structured light engineering[21]. This concept of spatially varying polarization transformation provides the basis for the simulation-based design discussed in Chapter 4.

2.4 Summary

This chapter establishes the theoretical and methodological foundation for the work presented in the subsequent chapters. It begins with the fundamental

description of polarization using Jones calculus and the Stokes–Mueller formalism. The roles of non-depolarizing polarization elements are then introduced to provide a physical understanding of polarization transformations. Building on this foundation, the principles of polarimetric measurement are presented. The chapter then reviews different types of polarimetric parameters, ranging from directly measured quantities to polarimetry basis parameters and higher-level feature parameters. Finally, the main application areas of polarization techniques are outlined. In particular, polarization-based characterization is reviewed with a focus on biomedical applications, while polarization modulation is introduced as a key approach for controlling the SoP of light. These sections provide a coherent framework for understanding polarization measurement, analysis, and applications, forming the basis for the concepts and experimental methods presented in the following chapters.

Chapter 3 Polarization information analysis in complex media

The contents of this chapter form the basis of the following publication: Elliptical vectorial metrics for physically plausible polarization information analysis. *Advanced Photonics Nexus* **4**(6), 066015 (2025). The work was carried out in collaboration with the co-authors of the publication. I made the main contribution to the research presented in this chapter, particularly through contributions to conceptualization, investigation, methodology, visualization, original drafting, and revision. Other co-authors helped with specific aspects of the work, such as experimental assistance, visualization, and manuscript review. The content has been adapted and extended for the purpose of this thesis, with material from the supplementary document of the manuscript and additional experimental details incorporated into this chapter.

3.1 Concept

Building on the foundation established in Chapter 2, this chapter advocates the use of a set of elliptical retarder (ER) parameters to characterize retarder samples with unknown structure, and evaluates its performance across different types of liquid crystalline samples.

3.1.1 Conventional decomposition

As outlined in Chapter 2, Mueller matrix polar decomposition (MMPD) is a widely used method for characterizing biomedical and optical materials, particularly through the retarder component[4,7,89]. Conventionally, the retarder matrix M_R is further decomposed into the product of a linear retarder (LR) matrix M_{LR} and a circular retarder (CR) matrix M_{CR}, as shown in the lower-left panel of **Figure 3.1**. Under this description, the retarder is characterized by three parameters: the linear retardance δ, the fast-axis orientation θ of the LR, and the circular retardance ϕ of the CR[54].

The above approach, however, may lead to misinterpretation when used to infer the physical properties of a retarder. As discussed in previous studies and revisited here, owing to its reciprocity and predefined form, the conventional parameters set can accurately represent the sample only when the retarder can be described as a CR followed by a LR[31,99]. In practice, many retarders, particularly in bulk biological tissues, exhibit complex multilayered structures for which detailed prior knowledge, such as the number of layers and the properties of each layer, is often unavailable. Moreover, some retarders do not possess a well-defined layered structure at all, making layer-based modelling inherently unsuitable. Without prior knowledge of the sample, treating the retarder as a fixed bilayer system may therefore produce misleading results. It is thus essential to adopt a parameter set

that can characterize retarder properties reliably without requiring assumptions about the underlying structure.

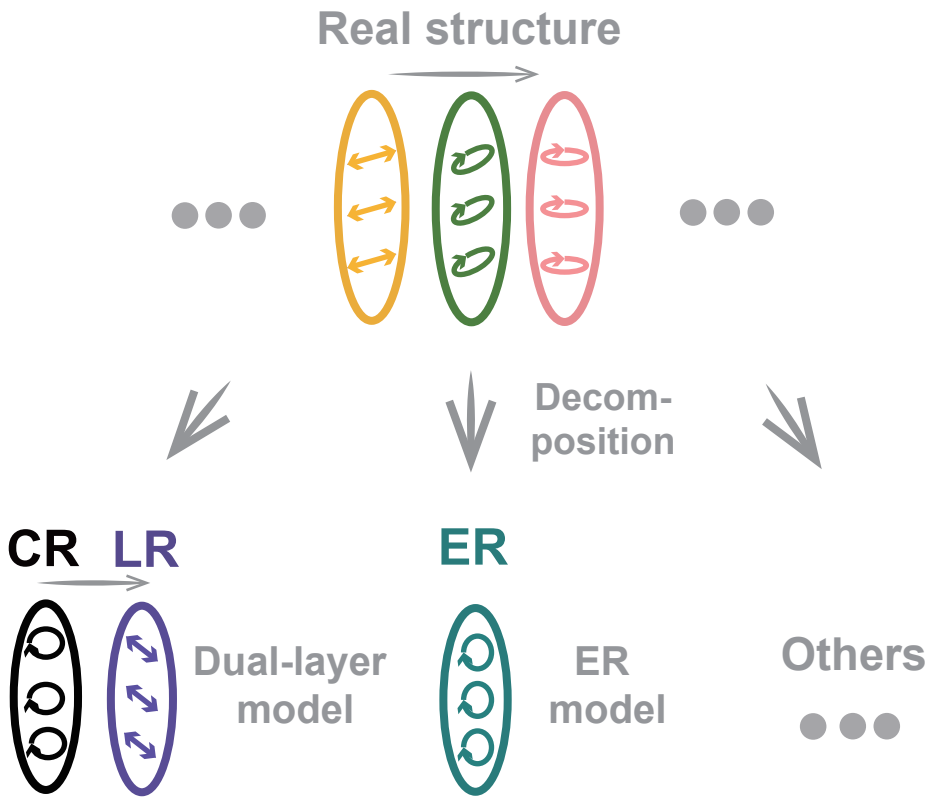


Figure 3.1. Real structure of a retarder and different characterization schemes. Circles, ellipses, and lines denote different fast-axis properties of each layer. The upper panel shows the real structure of a retarder, which may be multilayered or continuously varying. The lower-left panel illustrates the conventional dual-layer model, where the sample is represented by a CR followed by a LR. This predefined model may lead to misinterpretation of the polarization properties. The lower-middle panel shows the ER model, which characterizes an unknown sample as a single ER without assuming an underlying structure.

3.1.2 ER metrics for physically plausible analysis

For a retarder with an unknown internal structure, regardless of how complex the material may be, its overall action on polarized light can always be described as a single ER. The properties of the ER can be characterized by three parameters: the

elliptical axis orientation ϕ, the degree of ellipticity χ, and the elliptical retardance ρ.

The function of an ER can be seen as rotating along a specific axis on the Poincare Sphere (PS) by a certain angle. This rotation axis, which is by definition the fast axis of the retarder, corresponds to a particular polarization state U_R on the PS. According to the polarization ellipse formalism, this state is determined by two parameters: the elliptical axis orientation ϕ, defined in the range $[-\frac{\pi}{2}, \frac{\pi}{2}]$, and the degree of ellipticity χ, defined in the range $[-\frac{\pi}{4}, \frac{\pi}{4}]$. The fast axis of the retarder, S_R, and the corresponding polarization state U_R are given in Eq. (3.1), where a_1, a_2, and a_3 denote the three components of the normalized fast-axis vector. The parameters ϕ and χ can then be obtained from Eqs. (3.2) and (3.3), respectively.

$$S_R = \begin{pmatrix} 1 \\ a_1 \\ a_2 \\ a_3 \end{pmatrix} = \begin{pmatrix} 1 \\ \cos 2\varphi \cos 2\chi \\ \sin 2\varphi \cos 2\chi \\ \sin 2\chi \end{pmatrix} \quad U_R = \begin{pmatrix} \cos 2\varphi \cos 2\chi \\ \sin 2\varphi \cos 2\chi \\ \sin 2\chi \end{pmatrix} \tag{3.1}$$

$$\varphi = 0.5 \operatorname{atan2}(a_2, a_1) \tag{3.2}$$

$$\chi = 0.5 \sin^{-1} a_3 \tag{3.3}$$

The elliptical retardance ρ specifies the angle of rotation about that axis. Physically, ρ represents the phase shift introduced between the fast and slow axes as light propagates through the retarder. Its value can be calculated from the lower-right 3×3 submatrix of M_R, denoted by m_R, as given in Eq. (3.4).

$$\rho = \cos^{-1}\left[\frac{tr(m_R)-1}{2}\right] \tag{3.4}$$

The ER model described above was originally proposed by Lu and Chipman[7]. Building on this foundation, the key aim of this chapter is to show that, for a pure retarder system with no prior structural knowledge, the ER model not only provides an overall characterization of the system's polarization properties, but also helps avoid the potential misinterpretations that may arise from further decomposition.

3.2 Experimental validation

This section presents the experimental validation of the proposed elliptical concept using several different LC samples. Firstly, the experimental details are presented, including LC sample fabrication and data collection. Secondly, the limitations of the conventional dual-layer model are then examined for both layered and non-layered retarders. For layered samples, two experiments demonstrate the mismatch between the real structure and the results of the dual-layer model. Thirdly, the ER parameter set is then applied to all three cases introduced above. These results demonstrate the effectiveness of the ER approach for characterizing unknown retarders beyond the constraints imposed by conventional structural assumptions.

3.2.1 Experimental details

This section presents the experimental details, including LC sample fabrication and data collection. Firstly, the fabrication and structure of the LC samples used in this study are introduced. Secondly, the data collection process is described, including the experimental procedure, the collected data with representative simulated intensity images, and the data-processing methods.

3.2.1.1 LC sample fabrication

In the experiments, the LR was fabricated using a nematic LC mixture (E7, Synthon Chemicals Ltd., Wolfen, Germany) capillary-filled into a glass cell with anti-parallel rubbed polyimide alignment layers, as shown in **Figure 3.2**(a). The CR was fabricated using a chiral nematic LC mixture composed of 83 wt.% E7 and 17 wt.% R811 chiral dopant (Merck KGaA, Darmstadt, Germany), as shown in **Figure 3.2**(b)[100]. The air gap in the glass cell was 5 μm for the LR and 9 μm for the CR, as determined from UV–Vis transmission spectra. In the analysis, each LC glass cell is treated as a whole, and the optical effect of the glass substrates is assumed to be negligible.

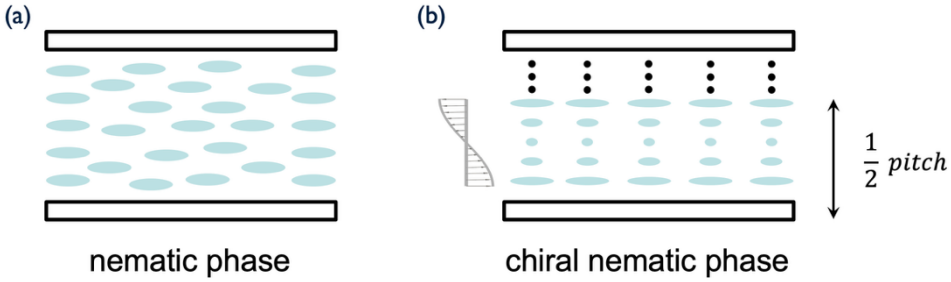


Figure 3.2. Illustration of LC glass cell for LRs and CRs. (a) Nematic LC for the LR, and (b) chiral nematic LC for the CR, with a half-pitch illustrated on the left side. The pitch refers to the distance over which the LC director, defined as the average molecular orientation, rotates by 360°. The black dots indicate continuation of the helical director structure beyond the representative half-pitch shown in the schematic.

Additionally, an LC droplet was fabricated as a non-layered sample, as shown in **Figure 3.3**. The LC droplet was composed of a chiral nematic LC mixture, containing 99 wt.% E7 LC and 1 wt.% R811 chiral dopant. Then, planar alignment layers were prepared by spin-coating a polyvinyl alcohol solution onto glass substrates, baking at 70°C for 30 seconds and rubbing to set a preferential alignment direction. Finally, LC droplets were printed onto the glass substrate/alignment layer with a MicroFab Jetlab II system equipped with an 80 μm nozzle MJ-AT-01-080-8MX printhead.

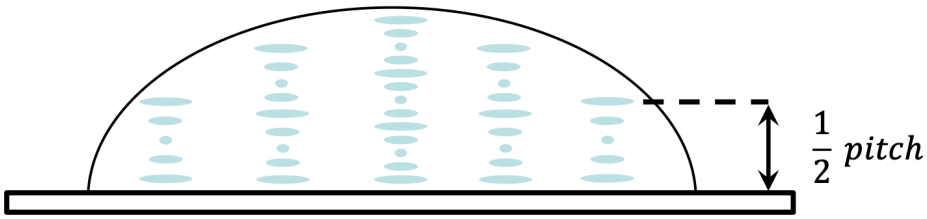


Figure 3.3. Illustration of chiral nematic LC droplet. The structure is composed of spatially varying, twisted LC director, rather than a layered configuration.

3.2.1.2 Data collection

In the data acquisition process, the experimental system used for collecting the data was the LC-based Mueller-matrix polarimeter presented in **Figure 2.1**. The LC sample was first placed on the microscope stage and brought into focus. The polarimeter was then initialized using the calibrated voltage–retardance relationships of the four liquid-crystal retarders. During each measurement, the four retarders were sequentially driven by predefined voltage combinations, producing 16 polarization measurement states. For each state, a monochrome intensity image of the sample was captured by the detector. A fixed region of interest was then selected from the recorded images for subsequent Mueller-matrix reconstruction.

For pixel-wise Mueller-matrix reconstruction, the 16 intensity values recorded at each pixel were arranged into an intensity vector, $\mathbf{i}(x, y)$. The corresponding Mueller matrix was reconstructed using the pseudoinverse of the 16×16 measurement matrix, which was determined by the predefined polarization measurement states:

$$\mathbf{m}(x, y) = \mathbf{A}^{+}\mathbf{i}(x, y). \tag{3.5}$$

Here, $\mathbf{A}^{+}$ is the pseudoinverse of the measurement matrix, and $\mathbf{m}(x, y)$ contains the 16 reconstructed Mueller-matrix elements at each pixel. The reconstructed

vector was then reshaped into a 4×4 Mueller matrix and normalized by its first element, M_{00}. Finally, an air-reference calibration was applied to reduce system-induced effects, producing the calibrated Mueller-matrix image for subsequent polarimetric parameter extraction.

At the detector level, each measurement generated 16 intensity images corresponding to the 16 polarization measurement states. In the original acquisition workflow, these images were used directly for pixel-wise Mueller-matrix reconstruction and were not archived separately as raw frames. Therefore, the raw detector intensity images for the reported measurements are not available. The retained data include the reconstructed normalized Mueller-matrix images and the derived polarimetric parameter maps. To illustrate the form of the 16-state measurements, representative simulated normalized intensity images are provided in **Figure 3.4**. These images were generated by applying the same forward measurement matrix to the reconstructed Mueller matrices. They are therefore not raw detector data, but serve as a transparent representation of the expected intensity images for the measurement states.

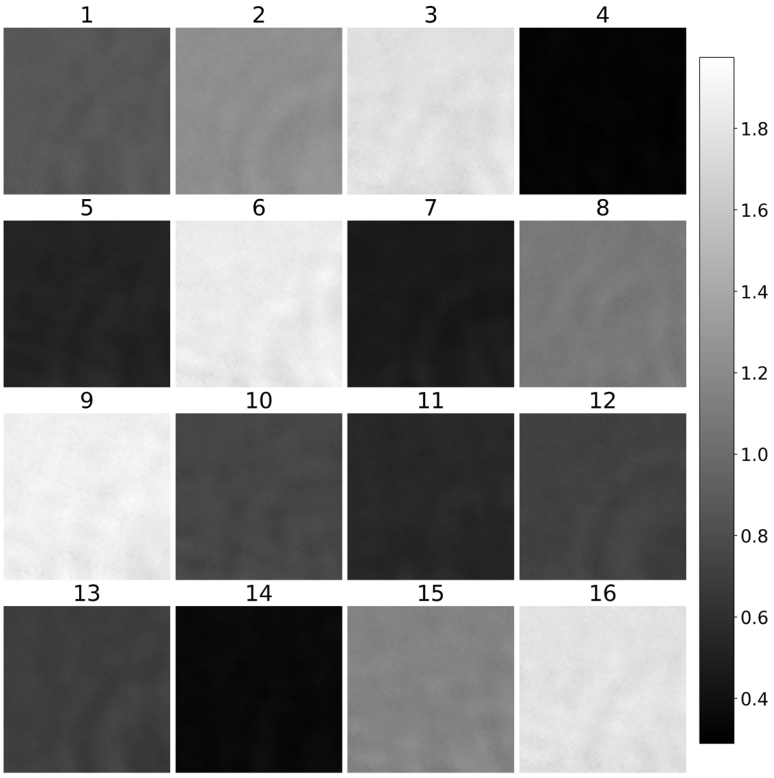


Figure 3.4. Simulated normalized intensity images under the 16 measurement states. The images were generated by applying the forward measurement matrix to the reconstructed Mueller matrices and are shown with a shared grayscale colour bar. These images are not raw detector frames, but illustrate the expected intensity measurements for the 16 polarization states.

After Mueller-matrix reconstruction, the normalized Mueller-matrix image was processed pixel by pixel using the MMPD method described in Section 3.1.1. This decomposition separates the measured polarimetric response into physically interpretable components, including diattenuation, depolarization and retardance-related parameters. The resulting parameter maps, including diattenuation, depolarization, linear retardance, linear fast-axis orientation, total retardance and circular retardance, were then used for subsequent visualization and analysis.

Notably, the measurements are expected to show limited wavelength dependence within a narrow spectral range around the operating wavelength. For the LC-based Mueller-matrix polarimeter, accurate reconstruction relies on the calibrated voltage–retardance relationship at the measurement wavelength. For small wavelength variations around the calibrated operating wavelength, the reconstruction is expected to remain broadly reliable; however, operation at a substantially different wavelength would require recalibration. For the LC samples, the absolute retardance may vary with wavelength because of material dispersion and the $1/\lambda$ dependence of phase retardance. However, the underlying director distribution and spatial organization of the sample are not expected to change significantly over a small wavelength range. Therefore, the main spatial features and the qualitative comparison between the conventional parameters and the elliptical-retarder parameters are expected to remain broadly consistent.

3.2.2 Limitations of layer-based decomposition model

3.2.2.1 Stacked linear–circular retarder sample

The first layered sample, denoted as Media A, consisted of a nematic LC cell acting as an LR followed by a chiral nematic LC cell acting as a CR, which together formed an overall ER ($M_R = M_{CR}M_{LR}$), as illustrated in **Figure 3.5**. The fabrication process of these two LC cells is described in **Section 3.2.1**. The reference parameters of the LR and CR components, together with the parameters

obtained from the conventional dual-layer model applied to the combined sample, were calculated over the full imaging area and are reported in **Table 1** as mean value $\pm$ standard deviation.

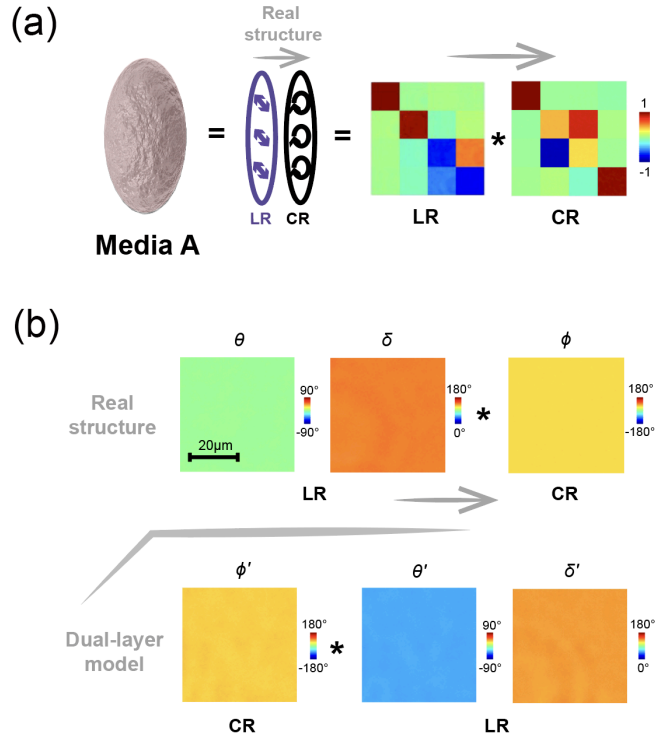


Figure 3.5. Comparison between the real structure and the result of the conventional dual-layer model for Media A. (a) Real structure of Media A and its corresponding Mueller matrix representation. Media A consists of a LR followed by a CR. **(b)** Comparison between the reference parameters of the real structure and the result obtained from the conventional dual-layer model. Although the model correctly retrieves the linear retardance δ and circular retardance ϕ, it yields an incorrect linear axis orientation θ.

The results show that the linear and circular retardances derived from the conventional model are close to the corresponding reference values. However, the linear axis orientation obtained from the conventional model deviates substantially from the reference, which may lead to misinterpretation. In

biomedical imaging, for example, such deviations could result in an incorrect inference of fibre orientation. Notably, in this special case, where the actual layer sequence of the sample is opposite to that assumed in the conventional dual-layer model, the conventional parameters can still yield the correct values of the linear retardance δ and circular retardance ϕ, whereas the linear axis orientation is shifted from θ to $\theta - 0.5\phi$. This experiment therefore demonstrates that when the layer sequence of the sample differs from the predefined model, the conventional parameter set can lead to misleading physical interpretation.

	Linear axis orientation θ	**Linear retardance δ**	**Circular retardance ϕ**
Reference	$0.541° \pm 0.409°$	$144.427° \pm 0.810°$	$64.986° \pm 0.300°$
	Circular retardance ϕ'	**Linear axis orientation θ'**	**Linear retardance δ'**
Dual-layer model	$70.614° \pm 1.287°$	$-36.605° \pm 0.342°$	$135.901° \pm 0.777°$

Table 3.1 Comparison of results between the reference and dual-layer model for the first sample (Media A).

3.2.2.2 Stacked-linear-retarder sample

The structure of the second sample, Media B, a nematic LC cell followed by another nematic LC cell, with both cells acting as LRs. Together, these two layers form an overall ER ($M_R = M_{LR2}M_{LR1}$), as shown in **Figure 3.6**. The fabrication process of these two nematic LC cells is described in **Section 3.2.1**. As before, the reference metrics of the two LR components, together with the metrics obtained by applying the conventional dual-layer model to the combined sample, were

calculated over the entire imaging area and are presented in **Table 3.2** as mean ± standard deviation.

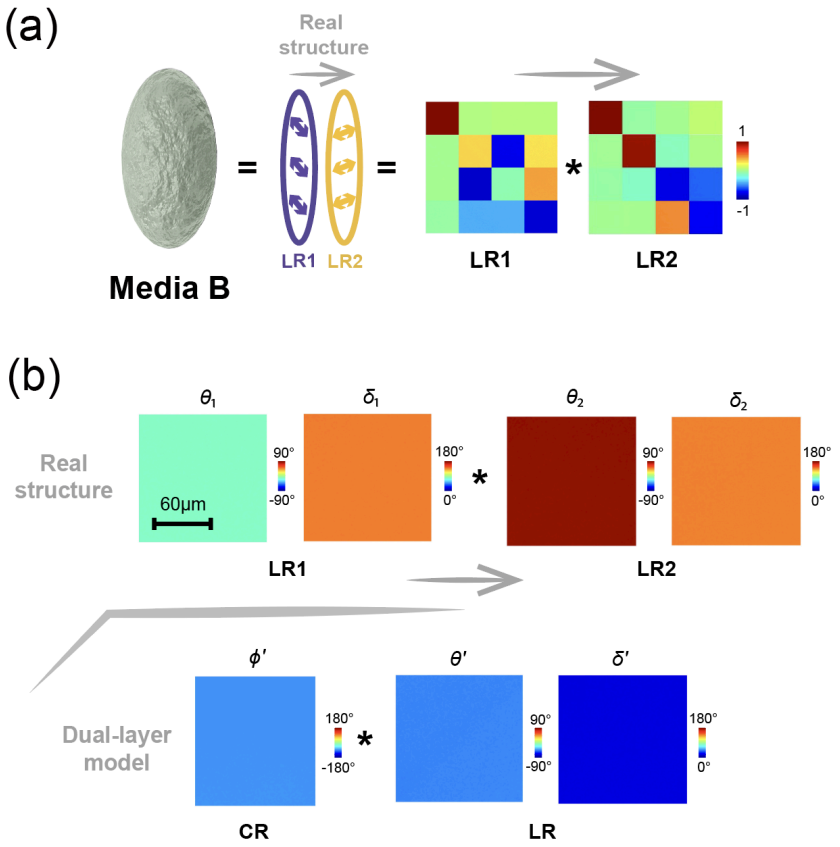


Figure 3.6. Comparison between the real structure and the result of the conventional dual-layer model for Media B. (a) Real structure of Media B and its corresponding Mueller matrix representation. Media B consists of two overlapping LRs with different axis orientations. **(b)** Comparison between the reference parameters of the real structure and the result obtained from the conventional dual-layer model. The conventional model fails to correctly recover the underlying structure.

	Linear axis orientation $\boldsymbol{\theta_1}$	**Linear retardance $\boldsymbol{\delta_1}$**	**Linear axis orientation $\boldsymbol{\theta_2}$**	**Linear retardance $\boldsymbol{\delta_2}$**
Reference	$-14.111° \pm 0.169°$	$142.969° \pm 0.242°$	$86.776° \pm 0.207°$	$142.277° \pm 0.316°$
	Circular retardance $\boldsymbol{\phi'}$	Linear axis orientation $\boldsymbol{\theta'}$	Linear retardance $\boldsymbol{\delta'}$	
Dual-layer model	$-84.755° \pm 0.348°$	$-44.846° \pm 0.469°$	$16.035° \pm 0.232°$	

Table 3.2 Comparison of results between the reference and dual-layer model for the second sample (Media B).

Comparison with the reference values shows that the conventional dual-layer model yields a CR with a large circular retardance ($\phi' = -84.755° \pm 0.348°$), even though no CR exists in the actual configuration. At the same time, it gives a linear retardance ($\delta' = 16.035° \pm 0.232°$) that is much smaller than the actual values. As in the previous experiment, these results demonstrate that conventional parameters may lead to misleading physical interpretations.

It should also be noted that some deviations are present in both experiments. We believe that these deviations may arise from three factors. First, the LC samples used here are not ideal LRs or CRs. Second, the total thickness of the stacked sample, including the glass substrates, is too large to allow fully accurate focusing, since each individual sample is 1.44 mm thick. Third, there is slight spatial non-uniformity in the LC distribution. During the measurement process, it is difficult to image exactly the same region in every measurement. Despite these deviations, the experimental results still support clear and convincing conclusions.

3.2.2.3 Non-layered LC droplet sample

The third sample, Media C, is an LC droplet that serves as an example of a non-layered sample, exhibiting a spatially varying and locally twisted director field

without well-defined macroscopic layering, as shown in **Figure 3.7**(a). The preparation process is described in **Section 3.2.1**. The measurements were performed using the imaging Mueller matrix polarimeter introduced in **Figure 2.1**, and the measured results were obtained across the field of view.

The results for Media C are shown in **Figure 3.7**(b). The upper row presents the ER parameters obtained from the measured Mueller matrices, including the elliptical-axis orientation ϕ, the degree of ellipticity χ, and the elliptical retardance ρ. For comparison, the lower row shows the parameters obtained using the conventional dual-layer model, giving an apparent CR parameter ϕ' and apparent LR parameters θ' and δ'. However, because Media C is a non-layered LC droplet with a spatially varying and locally twisted director field, these apparent CR and LR parameters should not be interpreted as real physical layers, and the conventional dual-layer model is inherently unsuitable for its characterization.

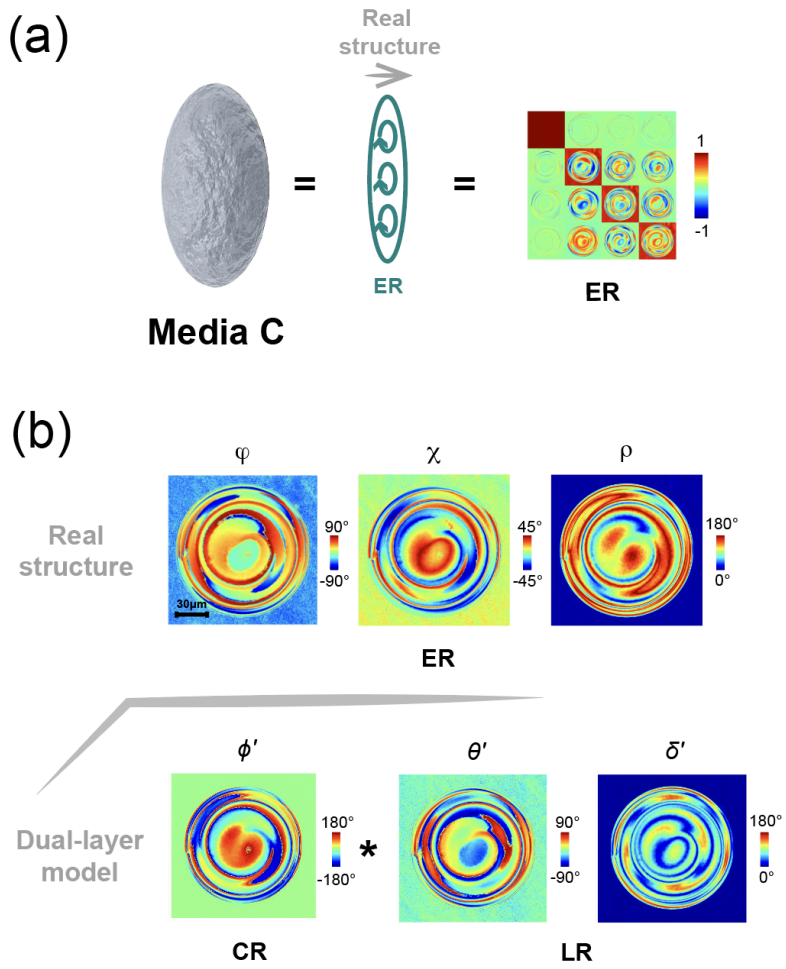


Figure 3.7. Comparison between the real structure and the result of the conventional dual-layer model for Media C. (a) Real structure of Media C and its corresponding Mueller matrix representation. Media C is an LC droplet with a spatially varying and locally twisted director field. **(b)** Comparison between the reference parameters of the real structure and the result obtained from the conventional dual-layer model. As a non-layered sample, Media C cannot be properly characterized within the conventional dual-layer framework.

3.2.3 Elliptical retarder-based characterization

To evaluate the effectiveness of the ER parameter set, we applied it to the three samples described above: two layered samples and one non-layered LC droplet sample. The purpose of this analysis was to demonstrate that the ER parameters

can provide a unified and physically reasonable description of retarder properties in both layered and non-layered samples.

First, media A, a layered sample composed of a LR followed by a CR, was re-examined, as shown in **Figure 3.8**. The distribution of the elliptical fast-axis orientation is shown in the middle panel of the figure. To provide a more intuitive visualization of the fast axis, sampled points within the region were used to plot the corresponding fast-axis ellipses. The results indicate that the fast axis is close to linear, with a low degree of ellipticity. The distribution of the elliptical retardance is shown in the right panel of the figure, with a mean value over the imaging region of $\rho = 143.830° \pm 1.205°$.

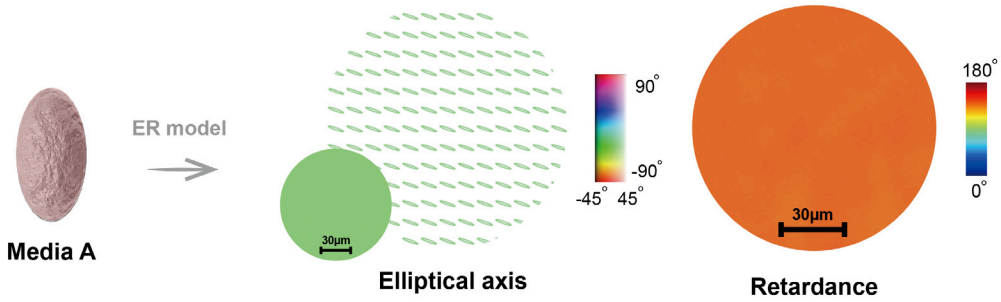


Figure 3.8. ER model characterization of Media A. Media A consists of a LR followed by a CR. The symbolic illustration of the sample is shown on the left. The middle panel shows the elliptical axis in the HSL representation, where hue denotes the orientation ϕ, luminance denotes the degree of ellipticity χ, and saturation is fixed at 1. For clarity, fast axes are evenly sampled from the imaging region and plotted as ellipses, whose colours follow the same encoding, and shapes represent the corresponding polarization states. The right panel shows the elliptical retardance distribution. The same format is used in **Figures 3.9** and **3.10**.

Second, media B, a layered sample composed of two LRs with different orientations, was re-examined, as shown in **Figure 3.9**. In this case, the sample exhibits a relatively high degree of ellipticity in its fast axis. The mean elliptical retardance over the imaging region was $\rho = 86.451° \pm 0.350°$. These optical properties are similar to those of a quarter-wave plate with a fast axis corresponding to left-handed circular polarization.

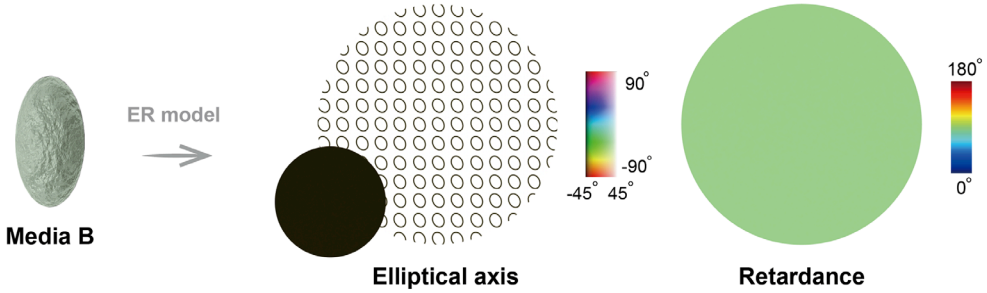


Figure 3.9. ER model characterization of Media B. Media B consists of two overlapping LRs with different orientations. The symbolic illustration of the sample is shown on the left. The middle panel presents the elliptical axis in the HSL representation, and the right panel shows the elliptical retardance distribution.

Third, media C, a non-layered LC droplet sample, was examined, as shown in **Figure 3.10**. The fast axis is found to exist predominantly in the form of elliptical polarization states. In particular, the central region is dominated by nearly right-handed elliptical polarization, whereas the peripheral regions exhibit more complex arrangements. In addition, the distribution of the elliptical retardance is consistent with that of the fast-axis orientation.

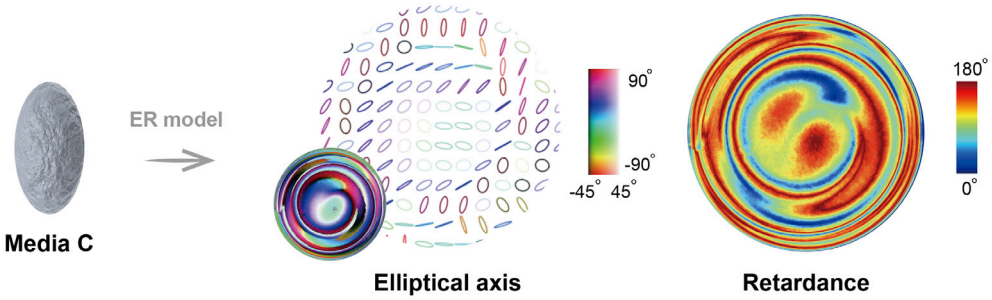


Figure 3.10. ER model characterization of Media C. Media C is an LC droplet with a spatially varying director field. The symbolic illustration of the sample is shown on the left. The middle panel presents the elliptical axis in the HSL representation, and the right panel shows the elliptical retardance distribution.

Together, these examples show that the ER parameter set can summarize the overall optical response as a single effective retarder, providing a physically reasonable description for both layered and non-layered samples. It avoids imposing an inappropriate layered interpretation while still providing spatially resolved maps of the local retarder properties. This supports the use of the ER model as a more general framework for characterizing samples with unknown or complex internal structures.

3.3 Discussion and summary

The choice of retarder decomposition method generally depends on prior knowledge of the sample. Without such prior information, no single decomposition method can be regarded as universally appropriate. To circumvent this limitation, we propose to use a set of ER parameters to characterize a retarder with unknown structure as a whole. This parameter set was originally introduced

by Lu and Chipman in 1996[7], where an arbitrary retarder was described in terms of its elliptical retardance and the corresponding fast axis. However, these parameters have seen limited use in current polarization analysis. In this work, we show that the ER parameter set is effective and, in many cases, more suitable for describing the polarization properties of samples.

Nevertheless, two additional issues must be considered if we want to uniquely describe a retarder. First, because of phase wrapping, a retardance range must be assumed, and the derived retardance values should be defined within that range. Second, even within a chosen retardance interval, for example from 0 to 2π, any given retarder has a corresponding retarder with different physical properties but the same Mueller matrix. The fast axis of this corresponding retarder is the slow axis of the given retarder, and its retardance is 2π minus the retardance of the given retarder. These ambiguities arise from the intrinsic limitations of the Stokes–Mueller formalism and may require additional prior knowledge of the sample, or the inclusion of other optical observables such as wavelength or absolute phase, to be resolved[101,102].

The significance of this work is not limited to the analysis of M_R within the MMPD framework. It can be extended to any pure retarder system, particularly in situations involving system-level modulation of polarized light. Compared with

the conventional decomposition model, this approach offers several advantages. First, it is well suited for the characterization of bulk biomedical samples, where the specimen often contains multiple layers with unknown internal structures[4]. Second, it is useful for characterizing waveplates or spatial light modulator arrays used in vector beam modulation, where the overall modulation effect of the system is important[18,19]. Third, recent studies have employed this set of parameters to construct physical fields with topological properties, suggesting potential applications in robust data storage area[103]. In summary, the ER parameter set provides a complementary perspective for characterizing media with complex or poorly defined structures. By representing the measured response as a single effective retarder, the ER model avoids imposing a predefined layered interpretation on the sample. This allows spatially resolved maps of retarder properties to be obtained even when the internal structure is unknown or not well described by simple layers. This improvement is therefore relevant to practical samples such as biological tissues and complex anisotropic materials, where the polarization response often arises from multilayered or heterogeneous structures.

Chapter 4 Simulation-based demonstration of multiplexed vector beam conversion using combined retarders and a diattenuator

The contents of this chapter form the basis of the following manuscript: Multiplexed vector beam conversion via complex structured matter. *arXiv preprint arXiv:2512.22980 (2025)*. The work was carried out in collaboration with the co-authors of the manuscript. I made the main contribution to the work, particularly through contributions to conceptualization, methodology development, simulation design and implementation, visualization, original drafting, and revision. Other co-authors helped with specific aspects of the work, such as methodology discussions, visualization, manuscript review, and revision. The content has been adapted and extended for the purpose of this thesis, with material from the supplementary document of the manuscript and additional simulation details incorporated into this chapter.

4.1 Concept

Building on the foundation established in Chapter 2, this chapter introduces a design framework for multiplexed vector beam conversion using combined

retarders and diattenuator and evaluates its performance through the manipulation of Stokes skyrmions.

4.1.1 Conventional methods for polarization modulation

Vector beams are a class of structured light whose polarization state varies spatially across the transverse beam profile[6,21,104]. Unlike uniformly linearly or circularly polarized light, they can exhibit complex polarization distributions, such as radial, azimuthal, or hybrid patterns. Owing to these distinctive properties, vector beams have attracted considerable interest in applications including optical communication[105,106] and optical computing.[107,108] As a result, the ability to manipulate vector beams with high flexibility and efficiency has become an important objective in structured-light research.

Existing passive devices for vector-beam manipulation mainly rely on optical retarders to control the state of polarization (SoP) of light, as reviewed in **Section 1.2**. Mathematically, a retarder-only device applies a unitary Jones transformation, or equivalently a rotation of the Stokes vector on the Poincaré sphere. Such transformations preserve the relative angular relationships between polarization states, and therefore cannot generally map several arbitrary input SoPs to independently prescribed output SoPs at the same pixel. As a result, retarder-only approaches are generally restricted to one prescribed input–output SoP conversion

at each pixel, which limits both the degree of control and the multiplexing capacity achievable within a single device. Recent developments in complex structured matter, particularly in metasurface[109,110]- and liquid crystal[111] (LC)-based platforms, have begun to expand the possibilities for polarization multiplexing. Nevertheless, important constraints remain, as the admissible input fields are often limited to orthogonal or otherwise predefined polarization states.

4.1.2 Cascade framework for multiplexed polarization conversion

To overcome the limitations of conventional passive devices, a design framework is introduced that enables a single passive element to simultaneously realize multiple polarization conversions between different input and output states. This strategy is referred to here as multiplexing, where the number of independent channels is defined by the number of input–output pairs supported by the device. As illustrated in **Figure 4.1**, the framework is implemented using complex structured matter composed of optical retarders and a diattenuator, and can support multiplexed polarization conversion for up to three channels.

For the three-channel case shown in **Figure 4.1**(a), each pixel of the device is designed to simultaneously satisfy three polarization mappings, converting the incident SoPs A, B, and C into their corresponding target output states A', B', and

C'. As highlighted by the red-marked pixel, the required transformation is defined locally at each spatial position. These input fields may be applied either sequentially in time or simultaneously at different wavelengths, depending on the implementation.

The corresponding device architecture is shown in **Figure 4.1**(b). It consists of three cascaded layers: a spatially varying retarder in the first layer, a horizontally aligned diattenuator with spatially varying transmission coefficients in the second layer, and a second spatially varying retarder in the third layer. The first and third layers are characterized by position-dependent retardance and fast-axis orientation, while the central diattenuator layer is fixed along the horizontal direction to simplify practical implementation.

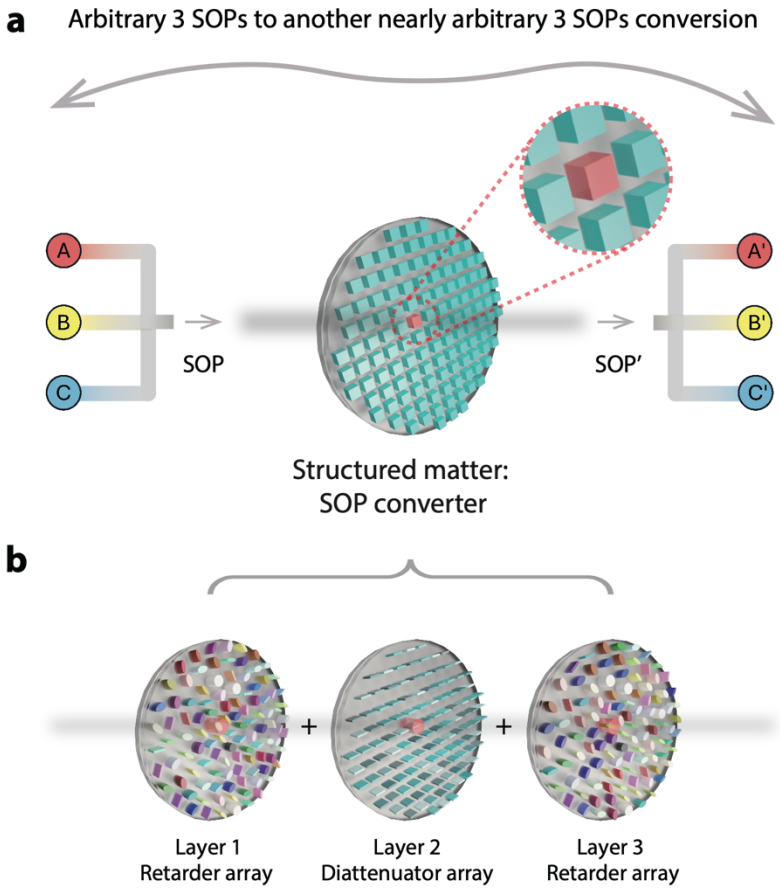


Figure 4.1. Functional illustration and layered structure of the converter. (a) Schematic of a three-channel converter. To realize transformations between three sets of input and output polarization fields, each pixel of the device is designed to map three incident SoPs to their corresponding output SoPs. As illustrated by the red-highlighted pixel, the incident polarization states A, B, and C are converted into the designed output states A', B', and C', respectively. These inputs can be applied either sequentially in time or simultaneously at different wavelengths. **(b)** Schematic of the three-layer converter structure. The first and third layers are retarder layers with spatially varying retardance and fast-axis orientation, while the second layer is a horizontal linear diattenuator with spatially varying transmission coefficients, which simplifies practical implementation. During operation, the incident SoP at each pixel is sequentially modulated by the retarder, diattenuator, and retarder at the corresponding positions in the three-layer structure, yielding the desired output SoP.

The role of the diattenuator can be understood by considering the inner product between two polarization states. For normalized Jones vectors, the magnitude of the inner product describes the overlap between the two states and is directly

related to their angular separation on the Poincaré sphere. For two input Jones vectors $E_{i,in}$ and $E_{j,in}$, after passing through a diattenuator J_D, the output inner product becomes

$$E_{i,out}^{\dagger}E_{j,out} = (J_D E_{i,in})^{\dagger}(J_D E_{j,in}) = E_{i,in}^{\dagger}J_D^{\dagger}J_D E_{j,in}. \quad (4.1)$$

Therefore, the matrix $J_D^{\dagger}J_D$ determines whether the relative relationship between different polarization states is preserved. If $J_D^{\dagger}J_D$ is proportional to the identity matrix, the inner products between states are preserved. However, for a horizontal linear diattenuator,

$$J_D = \mathrm{diag}(1, p),\ J_D^{\dagger}J_D = \mathrm{diag}(1, p^2), \quad (4.2)$$

which is not proportional to the identity when $p \neq 1$. As a result, the inner products, and therefore the relative angular relationships between different SoPs on the Poincaré sphere, are not generally preserved. This allows the diattenuator to reshape the arrangement of multiple intermediate states, while the surrounding retarders rotate the states before and after this reshaping step.

The geometric consequence can be understood more clearly from the Poincare Sphere (PS) representation shown in **Figure 4.2**. The first layer acts as an ER, rotating the incident SoPs into suitable intermediate states, as illustrated on the first PS. The second layer is a horizontal linear diattenuator, which modifies the relative positions of these intermediate SoPs so that they become compatible with those of the target outputs, as shown on the second PS. The third layer, also an

ER, then performs a further rotation to map the intermediate states onto the desired output SoPs, as illustrated on the third PS. In this way, the three-layer cascade enables each pixel to realize the prescribed multiplexed polarization transformation.

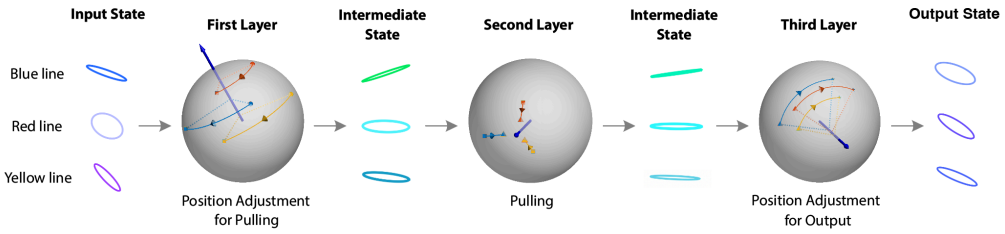


Figure 4.2. Functional interpretation of the three-layer converter. The transformations associated with each layer are illustrated sequentially on three PS. The blue, red, and yellow trajectories represent the SoP evolution through the first, second, and third layers, respectively, as indicated on the left side of the figure. The first layer, an ER, rotates the input states into an intermediate configuration. The second layer, a horizontal linear diattenuator, modifies the relative positions of these states. The third layer, another ER, further rotates the intermediate states to the desired output SoPs.

4.1.3 Implementation of the framework

For implementation of the framework, an analytical method is proposed for the two-channel case, and a numerical method is proposed for three-channel multiplexing.

4.1.3.1 Analytical method

For the two-channel multiplexing case, an analytical method is proposed to directly determine the device parameters. This approach offers two main

advantages: clear physical interpretability and low computational cost, as it explicitly reveals the role of each optical element in the transformation process and avoids iterative optimization.

For a two-channel converter, each pixel is required to satisfy two specified SoP transformations. Consider two distinct input SoPs $\overrightarrow{S_A}$ and $\overrightarrow{S_B}$, and their corresponding output states $\overrightarrow{S_1}$ and $\overrightarrow{S_2}$. To determine the transmission coefficient p of the diattenuator, let ζ denote the central angle between the two input states, and ξ denote the central angle between the two output states.

For simplicity, the first layer, an ER, is designed to rotate $\overrightarrow{S_A}$ and $\overrightarrow{S_B}$ to the following intermediate Stokes vectors:

$$\overrightarrow{S'} = \begin{pmatrix} 1 \\ \cos(\pi - \frac{\zeta}{2}) \\ 0 \\ \pm\sin(\pi - \frac{\zeta}{2}) \end{pmatrix} \tag{4.3}$$

where the $\pm$ sign corresponds to $\overrightarrow{S_A}$ and $\overrightarrow{S_B}$, respectively. Since the angle between the input and output Stokes vectors remains unchanged, Euler's rotation theorem guarantees the existence of a corresponding rotation and allows the determination of the rotation axis and angle.

Then, the second layer, a horizontal linear diattenuator, transforms the intermediate state $\overrightarrow{S'}$ into

$$\overrightarrow{S''} = \begin{pmatrix} 1 \\ \cos(\frac{\xi}{2}) \\ 0 \\ \pm\sin(\frac{\xi}{2}) \end{pmatrix} \tag{4.4}$$

After this step, the angle between the two polarization states changes from ζ to ξ. The transmission coefficient p of the diattenuator must satisfy the following equation:

$$\overrightarrow{S''} = M_D\overrightarrow{S'} = \frac{1}{2}\begin{pmatrix} 1+p^2 & 1-p^2 & 0 & 0 \\ 1-p^2 & 1+p^2 & 0 & 0 \\ 0 & 0 & 2p & 0 \\ 0 & 0 & 0 & 2p \end{pmatrix}\begin{pmatrix} 1 \\ \cos(\pi-\frac{\zeta}{2}) \\ 0 \\ \pm\sin(\pi-\frac{\zeta}{2}) \end{pmatrix} \propto \begin{pmatrix} 1 \\ \frac{1-p^2+(1+p^2)\cos\left(\pi-\frac{\zeta}{2}\right)}{1+p^2+(1-p^2)\cos\left(\pi-\frac{\zeta}{2}\right)} \\ 0 \\ \pm\frac{2psin\left(\pi-\frac{\zeta}{2}\right)}{1+p^2+(1-p^2)\cos\left(\pi-\frac{\zeta}{2}\right)} \end{pmatrix} \tag{4.5}$$

where M_D denotes the Mueller matrix of the horizontal linear diattenuator, and $\overrightarrow{S'}$ and $\overrightarrow{S''}$ denote the specified input and output polarization states, respectively. Substituting Eq. (4.4) into Eq. (4.5) yields an explicit expression for p:

$$p = \sqrt{\frac{[\cos\left(\frac{\zeta}{2}\right)-1][\cos\left(\frac{\xi}{2}\right)-1]}{[\cos\left(\frac{\zeta}{2}\right)+1][\cos\left(\frac{\xi}{2}\right)+1]}} \tag{4.6}$$

Finally, the third layer, another ER, rotates the intermediate states $\overrightarrow{S''}$ to the target output states $\overrightarrow{S_1}$ and $\overrightarrow{S_2}$. As the diattenuator has already adjusted their relative geometry, the angular separation between $\overrightarrow{S''}$ matches that of the target outputs. Therefore, by Euler's rotation theorem, the required rotation always exists, and the corresponding rotation axis and angle can be determined.

4.1.3.2 Numerical method

For three-channel multiplexing, the analytical method is no longer directly applicable. To address this, a general numerical design method is adopted for the three-channel converter and above, and its workflow is illustrated in **Figure 4.3**.

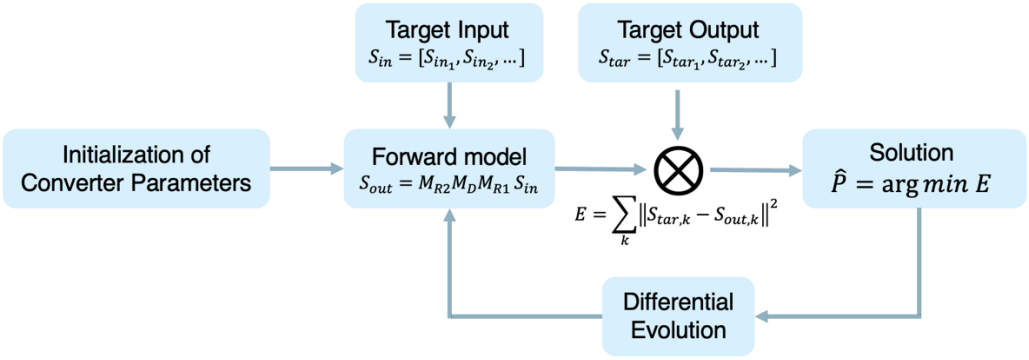


Figure 4.3. Workflow of the numerical design method. The forward model describes the Mueller matrix of each pixel, determined by the fast-axis orientation and retardance of the two retarder layers, together with the transmission coefficient p of the horizontal linear diattenuator layer. The parameters are initialized using Latin hypercube sampling. For each parameter set, the model takes the target input vectors and calculates the corresponding output vectors. A differential evolution algorithm is then used to iteratively update the parameters by minimizing the squared geometric distance between the simulated and target output vectors.

The numerical design procedure is summarized as follows: (1) A forward model is first constructed for each pixel based on the Mueller matrix of the three-layer converter. As shown on the left side of **Figure 4.3**, the model parameters include the fast-axis orientation and retardance of the first and third retarder layers, together with the transmission coefficient p of the second-layer horizontal linear diattenuator. (2) These parameters are initialized using Latin hypercube sampling. (3) The forward model takes the input Stokes vectors and computes the corresponding output vectors for the current parameter set. (4) An error function is then defined as the sum of the squared Euclidean distances between the

calculated output vectors and their corresponding target vectors across all input–output pairs, as illustrated in the centre of the figure. (5) A differential evolution algorithm is employed to iteratively optimize the parameters by minimizing this error. The final design of each pixel is given by the parameter set that yields the minimum total distance, as shown on the right side of **Figure 4.3**. All examples presented in the following sections were obtained using this method.

4.2 Framework demonstration via Stokes skyrmion multiplexing

To demonstrate the effectiveness of the proposed foundation, two multiplexing devices are designed and analysed: a Stokes skyrmion generator and a converter. Stokes skyrmions are optical counterparts of the topological quasiparticles originally introduced by Tony Skyrme in 1962[112]. It exhibits characteristic topological textures that encode a discrete and topologically protected number[16,113–116]. These properties make it particularly attractive for on-chip photonic integration and information processing[117], and therefore provide a suitable platform for demonstrating the application potential of passive polarization multiplexing.

The design and verification procedure for the two devices is summarized as follows. (1) According to the target functionality of each device, three sets of input

polarization fields and their corresponding output fields are defined. (2) Based on these field pairs, the required SoP transformations at each pixel are determined. (3) The corresponding retarder and diattenuator parameters of each pixel are then calculated using the numerical design method described in **Section 4.1.3.2**. (4) Finally, the Mueller matrix array of the designed device is constructed and applied to the incident polarization fields to verify whether the resulting outputs agree with the target fields. The following sections present these two device designs in detail and examine the multiplexing capacity of the framework.

4.2.1 Three-channel skyrmion generation

As a first demonstration, a three-channel skyrmion generator is designed to generate three different Néel-type skyrmions under three distinct uniform incident polarization fields. The configuration of the generator is shown in **Figure 4.4**.

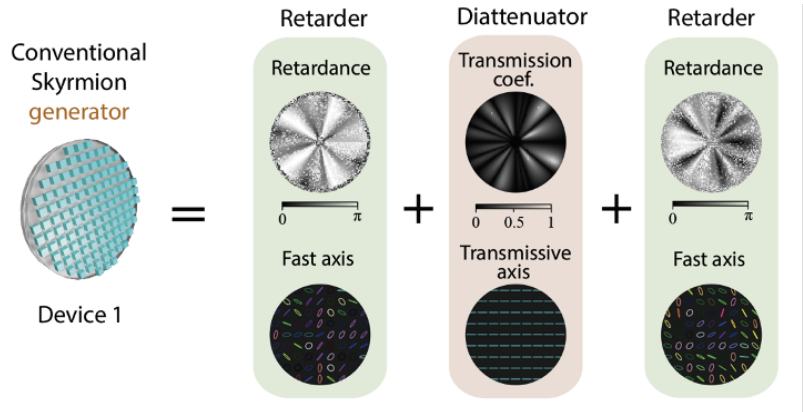


Figure 4.4. Structure of the time-division skyrmion generator. The generator consists of three layers. The first and third layers are retarders with spatially varying distributions of retardance and fast-axis orientation, while the second layer is horizontal linear diattenuators with spatially varying transmission coefficient and axes. For clarity, the

axes are represented by polarization ellipses and shown as hollow symbols (using the same notation as in Chapter 3).

Its performance under time-division operation is presented in **Figure 4.5**. Specifically, at t_1, a 0° linearly polarized input is converted into a conventional Néel-type skyrmion with skyrmion number (SkyN) $= 1$; at t_2, a 45° linearly polarized input is converted into a conventional Néel-type skyrmion with SkyN $= 5$; and at t_3, a right-circularly polarized input is converted into a conventional Néel-type skyrmion with SkyN $= 10$. This example demonstrates that the proposed framework can support multiplexed skyrmion generation within a single passive device, thereby increasing functional flexibility while reducing the need for device reconfiguration.

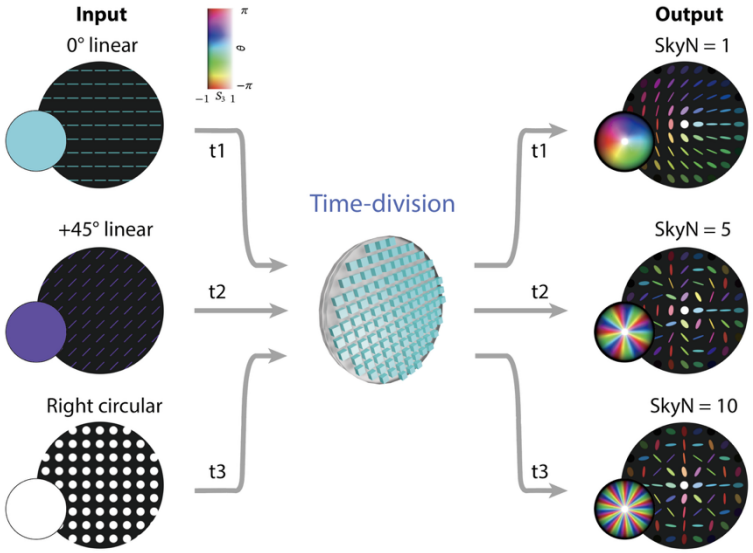


Figure 4.5. Performance of the time-division skyrmion generator. Three uniform input fields—0° linear, 45° linear, and right-circular polarization—are converted into Néel-type skyrmions with SkyN $= 1$, 5, and 10, respectively. These inputs may be applied in different time slots, corresponding to time-division multiplexing. Throughout this chapter, Stokes fields are visualized with hue representing the azimuthal angle

θ ($\tan\theta = S_2/S_1$) and saturation representing the S_3 component, as indicated by the colour bar at the upper left. To aid interpretation, the corresponding polarization ellipse distributions are also shown; the ellipse colors match the local Stokes parameters, while their shapes represent the local SoP.

4.2.2 Three-channel skyrmion converter

As a second demonstration, a passive skyrmion converter is designed to perform three independent conversions between pairs of Stokes skyrmions at different wavelengths. The configuration of the converter is shown in **Figure 4.6**.

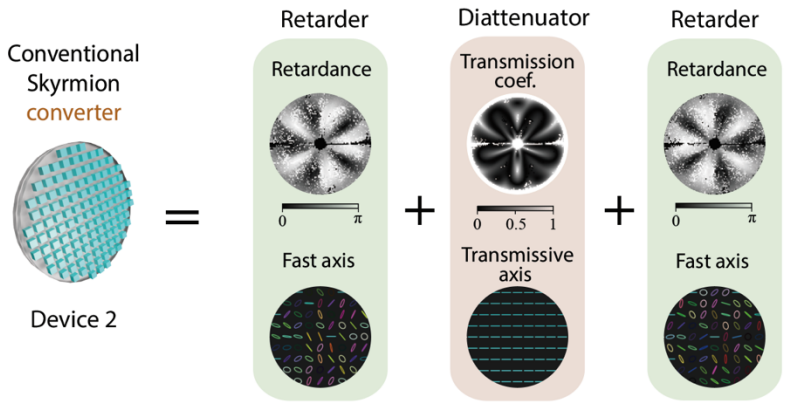


Figure 4.6. Structure of the wavelength-division skyrmion converter. The converter consists of three layers, namely two retarder layers and one intermediate diattenuator layer. The corresponding properties of the three layers are shown.

Its performance under wavelength-division operation is presented in **Figure 4.7**, where the three conversions are assigned to three wavelength channels λ_1, λ_2, and λ_3. Specifically, at wavelength λ_1, a skyrmion field with SkyN $= 1$ and a left-circular boundary is converted into a field with SkyN $= 5$; at λ_2, a field with SkyN $= 5$ and a right-circular boundary is converted into a field with SkyN $= 1$;

and at λ_3, a field with SkyN $= 5$ and a $-45°$ linear boundary is converted into a field with SkyN $= -5$. In all three cases, the boundary conditions are preserved during the conversion process.

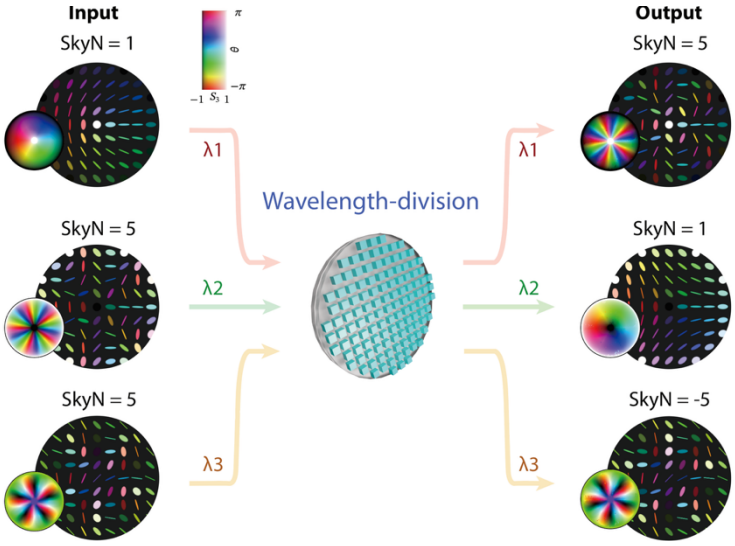


Figure 4.7. Performance of the wavelength-division conventional skyrmion converter. Three input skyrmion fields are converted into their respective output skyrmion. The three input fields are: a skyrmion with SkyN $= 1$ and left-circular boundary conditions (top), a skyrmion with SkyN $= 5$ and right-circular boundary conditions (middle), and a skyrmion with SkyN $= 5$ and $-45°$ linear boundary conditions (bottom). These fields are converted into output skyrmions with SkyN $= 5$, 1, and -5, respectively, while preserving the boundary polarization states. The three inputs may be applied at different wavelength channels.

These results further demonstrate that the proposed framework can realize multiplexed transformations between distinct skyrmions within a single passive device. Since such transformations can represent changes in encoded information, this multiplexed conversion capability may be valuable for parallel information processing in optical computing.

4.2.3 Error analysis and multiplexing capacity

The two examples above all employ three-channel multiplexing. This naturally raises two further questions: (1) whether three-channel multiplexing can be achieved reliably, and (2) whether it represents the upper limit of the multiplexing capability of the proposed framework. To address these questions quantitatively, the pixel error is defined as the sum of the squared Euclidean distances between the actual output Stokes vectors and their corresponding target vectors over all SoP pairs.

$$E_{pixel} = \sum_k \left\| S_{tar,k} - S_{out,k} \right\|^2, \; S_{out,k} = M_{R_2} M_D \, M_{R_1} S_{in,k}. \tag{4.7}$$

The spatial distributions of the pixel error for the two designs are shown in **Figure 4.8**. In both designs, most pixels have near-zero error and therefore appear black in the maps. The non-zero errors are confined to a small number of isolated pixels or narrow regions, rather than being distributed across the whole device. This indicates that the designed transformations are successfully realized over almost the entire field of view.

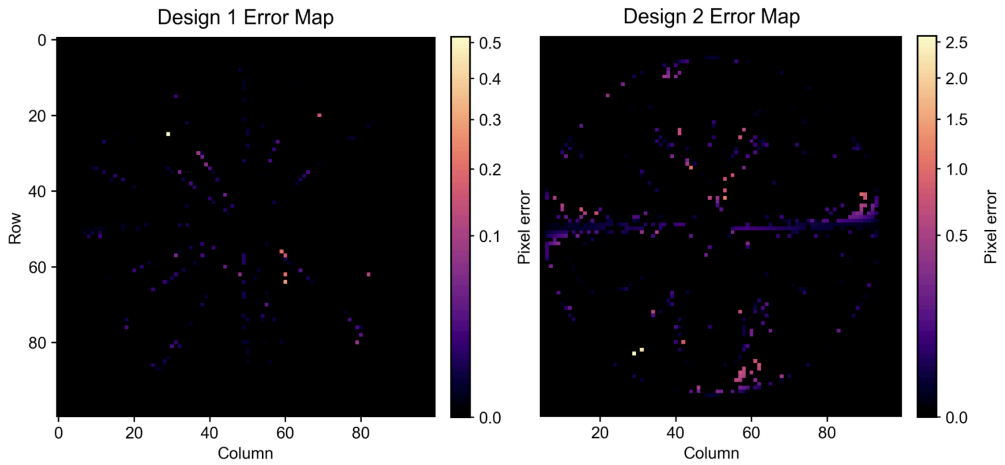


Figure 4.8. Pixel-error maps for the two designs. The pixel error is calculated at each spatial position by summing the squared Euclidean distances between the target and actual output Stokes vectors over all input–output SoP pairs. Most pixels show near-zero error and appear black, while only a small number of localized pixels exhibit larger errors. The two maps use separate colour scales to make the sparse high-error pixels visible.

The reliability of three-channel multiplexing is further examined. As shown in **Figure 4.9**(a), the blue and orange curves represent the pixel-error distributions for devices 1 and 2, respectively. Although a very small fraction of pixels exhibits errors above 10^{-4}, as indicated by the right arrow in **Figure 4.9**(a), the vast majority of pixels have errors below 10^{-16}, as marked by the left arrow. This result indicates that the designed polarization transformations are realized with high numerical accuracy.

The multiplexing capacity of the framework is then evaluated by comparing error distributions obtained from random trials with two to five channels, as shown in **Figure 4.9**(b). For two- and three-channel multiplexing, nearly all simulations yield errors below 10^{-15}, with most below 10^{-17}, confirming the high precision

and robustness of the framework within this range. In contrast, for four- and five-channel cases, the errors increase substantially, with median values exceeding 10^{-1}. These results indicate that the proposed converter design can support high-precision polarization multiplexing up to three channels but is not suitable for higher-channel operation.

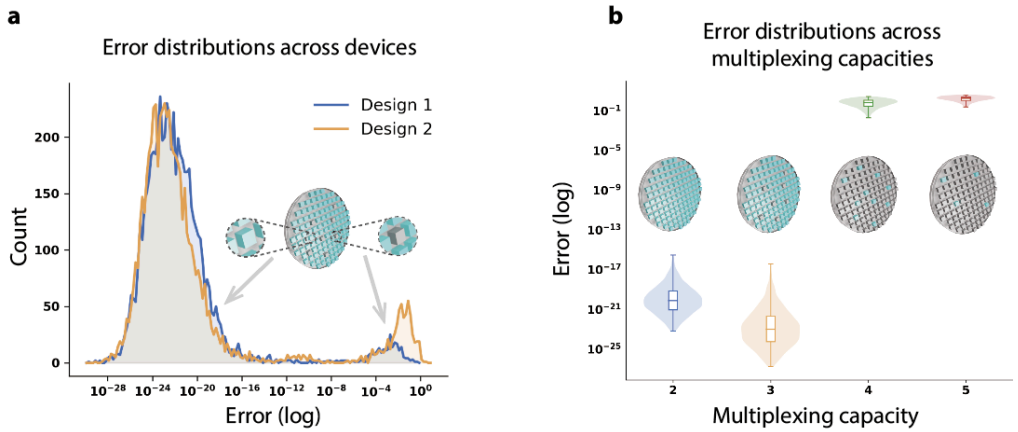


Figure 4.9. Design error analysis and capacity evaluation. (a) Pixel-error distributions for the two device designs shown in **Figure 4.4** and **Figure 4.6**, where the blue and orange curves correspond to devices 1 and 2, respectively. The horizontal axis represents the pixel error, and the vertical axis represents its probability density. For these two devices, although a small number of pixels exhibit relatively large errors exceeding 10^{-4} (indicated by the right arrow), the majority of pixel errors are below 10^{-16} (indicated by the left arrow), demonstrating that the designed functionalities are realized with high accuracy. The schematic in the centre illustrates this distribution qualitatively: a small number of failed pixels are shown in grey, whereas most pixels are shown in blue, indicating successful performance. **(b)** Error distributions obtained from 5000 independent numerical trials for channel numbers ranging from 2 to 5. In each box plot, the box spans the 25th to 75th percentiles, with the central line indicating the median. The whiskers extend to the 2nd and 98th percentiles, and outliers are omitted. The surrounding shaded profiles indicate the density of the error values. Most errors for two- and three-channel converters are below 10^{-15}, whereas the errors for four- and five-channel cases are substantially larger. This indicates that the proposed design supports high-precision polarization multiplexing up to three channels but is not suitable beyond this range.

4.3 Discussion and summary

This chapter has introduced a design framework for multiplexed polarization conversion based on a three-layer structured medium composed of a diattenuator layer sandwiched between two retarder layers. Within this framework, a single passive device can be designed to simultaneously realize multiple input–output polarization transformations, enabling the implementation of diverse functionalities in a compact and unified manner.

The motivation for developing this framework is that passive multiplexed conversion can reduce the need for active switching or multiple separate optical elements, and increase the number of polarization-encoded channels handled by a single component. When applied to skyrmionic fields, as demonstrated in this chapter, this capability is particularly attractive because polarization fields can be used to encode different information, with potential applications in optical communication and optical computing. The proposed framework therefore provides a potential route toward more parallel, compact, and energy-efficient integrated optical computing chips.

Two main advantages of the proposed framework can be identified. First, it enables multiplexed operation, supporting up to three independent polarization transformation channels within a single device. This significantly enhances

functional density compared to conventional approaches that are typically limited to a single transformation. Second, both the input and output Stokes profiles can be tailored with a high degree of flexibility, allowing the framework to be readily adapted to a wide range of polarization-based applications beyond the skyrmions examples demonstrated in this work.

Despite these advantages, several limitations remain. From an implementation perspective, the design requires precise control over both spatially varying retarders and diattenuators. For spatially varying retarders, different physical implementation routes are possible. One flexible approach is to synthesize the desired retarder distribution by cascading simple spatially programmable retarders, such as liquid-crystal spatial light modulators[18,19]. In this case, each individual layer provides a limited set of controllable retardance or fast-axis responses, while the cascade can generate a more general spatially varying retarder response. This provides a reconfigurable implementation route, although it may require multiple optical elements and careful alignment. Alternatively, the required retarder distribution could be directly encoded into a fabricated optical element, such as metasurfaces[13,118]. Recent advances in metasurfaces have demonstrated strong control over local birefringence, suggesting a more compact but typically less reconfigurable route for implementing spatially varying retarders.

For diattenuators, achieving spatially varying diattenuation remains challenging. In this framework, the fabrication complexity of the diattenuator is partially alleviated by constraining its principal axis to horizontal linear polarization, enabled by the additional retarder layer[7]. Furthermore, emerging metasurface technologies provide promising routes for realizing diattenuators with spatially varying transmission coefficients, suggesting that practical implementation may become feasible with continued advances in nanofabrication[119,120].

Additionally, the device response is expected to show wavelength dependence, because retardance and diattenuation may vary with wavelength. For small wavelength variations around the design wavelength, changes in the device parameters may be tolerable. This is particularly relevant for the skyrmion-based examples in this chapter, where the topological structure is expected to be robust against small perturbations. As a result, the designed function may remain stable. However, for substantially different wavelengths, the device parameters may change significantly, and the original design may no longer produce the intended conversion accurately. In that case, recalibration or redesign would be required. Alternatively, the wavelength dependence could be treated as an additional design degree of freedom: different wavelengths could be modelled as different effective device responses and incorporated into the optimization framework to achieve different multiplexed functionality.

A further practical factor is the illumination geometry. The present demonstrations are based on the normal-incidence approximation, in which each pixel is described by an effective Mueller response of the designed cascade. Under oblique illumination, this effective response may change because the effective retardance and polarization-dependent transmission can become angle dependent. Therefore, the output Stokes fields are expected to deviate from the normal-incidence design, particularly for large incident angles or high-numerical-aperture illumination. For small angular deviations, however, these changes are likely to act mainly as perturbations to the designed response. This is again relevant for the skyrmion-based examples considered in this chapter, where the topological structure may remain stable as long as the perturbation does not drive the field across a topological transition. For strongly oblique illumination, recalibration or redesign would be required. More generally, such angle-dependent effects could be incorporated into the same optimization framework by replacing the normal-incidence Mueller response with an angle-dependent response function and optimizing over the required angular range.

From a theoretical perspective, the framework is fundamentally based on the linear Mueller–Stokes formalism, which imposes an upper limit on the number of independent transformation channels. As demonstrated in this work, high-

precision multiplexing can be achieved for up to three channels, whereas performance degrades significantly beyond this range. In addition, certain specific transformation configurations may not be realizable within the current framework. However, for many practical applications, particularly those involving topological polarization structures such as skyrmions, these limitations are not critical. The inherent topological protection of such fields ensures that small local deviations do not affect the global structure, thereby maintaining functional robustness.

Looking forward, several possible directions may extend the capability of the proposed framework. Incorporating noise engineering and error-tolerant design strategies may enable reliable operation with a higher number of channels[121–123]. In addition, extending the framework beyond linear optics, for example by introducing nonlinear optical responses, may expand the achievable multiplexing capacity[124–126].

In summary, the proposed framework demonstrates that a single passive device can perform multiple polarization transformations that would traditionally require either reconfigurable systems or multiple optical components. This capability offers a pathway toward reducing system complexity while enabling compact and highly integrated implementations. As vectorial light continues to play an increasingly important role in areas such as optical communication, computation,

and information processing, the multiplexing strategy developed here provides a flexible and scalable approach for next-generation polarization-based photonic systems.

Chapter 5 Conclusion and future work

5.1 Conclusion

This thesis is centred on the Mueller matrix and explores how Mueller-matrix-based polarimetric parameters can be used to analyse polarization-related light–matter interactions and to support the design of polarization-based functionalities built upon them. In particular, it focuses on two closely connected directions: the physically meaningful interpretation of retarder-related parameters, and the extension of this perspective to combined retarder–diattenuator systems for polarization control and modulation.

The first part of this thesis examined how retarder information should be described when the internal structure of a sample is unknown. Although the conventional decomposition of the retarder matrix is mathematically valid, it may lead to physically misleading interpretations when the actual sample structure differs from the assumed layered model. To address this issue, this thesis advocated the use of ER parameters to characterize an unknown retarder. Experiments on layered and non-layered liquid crystal (LC) samples revealed that this parameter set provides a more physically plausible description of retarder properties in complex media. This result demonstrates that the choice of parameterization is critical for obtaining a physically plausible description of polarization properties.

Building on the analysis of pure retarder systems, the second part of the thesis extended the discussion to optical systems containing both retarders and diattenuators. In this context, the Mueller matrix serves not only as a foundation for characterization, but also as a foundation for design. A three-layer cascade consisting of a retarder, a diattenuator, and a retarder was introduced to realize multiplexed vector beam conversion within a single passive device. Analytical and numerical methods were developed for two-channel and three-channel operation, respectively. The framework was then demonstrated through the manipulation of Stokes skyrmions. These results demonstrate that the proposed framework enables up to three-channel multiplexed vector beam conversion within a single passive device.

Together, these two studies show that polarimetric parameters in the Mueller matrix are not merely quantities extracted from measurement but can also serve as effective descriptors and design variables for understanding light–matter interactions and supporting polarization-based optical design. From retarder-related parameter analysis to retarder–diattenuator-based polarization conversion, this thesis therefore establishes a coherent route linking polarization information analysis and polarization modulation under a unified Mueller matrix perspective.

5.2 Future work

This section outlines future research directions that naturally follow from this thesis, as illustrated in **Figure 5.1**. Looking beyond the retarder-related and retarder–diattenuator systems studied here (purple layer), the next step is to investigate more complete sets of Mueller-matrix-derived properties and their potential to be used together with non-polarimetric parameters in practical applications. This progression may be developed in two successive stages: (1) to extend the analysis from the nondepolarizing regime to full polarimetric information by incorporating depolarization (blue layer); and (2) to further combine these richer polarimetric descriptions with broader forms of information such as morphological, chemical, and other non-polarimetric parameters (orange layer), for more advanced analysis and practical problem solving. Overall, these two stages describe a progression from nondepolarizing properties to full polarimetric information, and then to its broader integration with other forms of information.

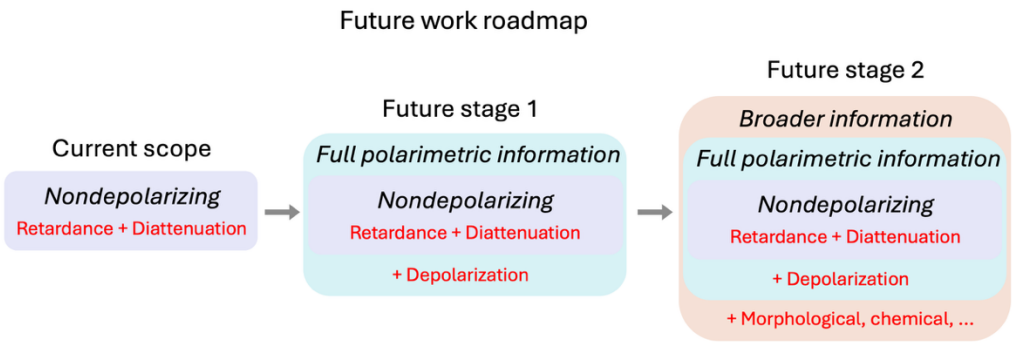


Figure 5.1 Future research directions. The present work mainly focuses on the nondepolarizing regime, characterized by retardance and diattenuation (purple layer). Future stage 1 extends this description to full polarimetric information by incorporating depolarization (blue layer). Future stage 2 further broadens the framework by combining

polarimetric information with other forms of information, such as morphological and chemical parameters, for more advanced analysis and practical applications (orange layer).

5.2.1 Joint interpretation of polarimetric parameters

A natural direction for future work is to move beyond the interpretation of individual nondepolarizing parameters and extend the analysis toward full polarimetric information. In real samples, retardance, diattenuation, depolarization, and related Mueller-matrix-derived quantities often coexist and reflect different but connected aspects of the underlying microstructure. A more complete structural characterization may therefore require not only extracting these parameters individually, but also understanding how they are related to one another and how they should be interpreted jointly[4].

One motivation for this direction comes from transmission-mode applications. In thin sections and weakly scattering samples, retardance and axis orientation are already widely used together to characterize aligned microstructures[127]. In addition, a recent Achilles tendon study reported lower retardance and larger diattenuation in injured tissue[128]. The need for joint interpretation becomes even stronger in reflection-mode applications, where depolarization plays an important role. In highly scattering samples, the polarization response is influenced by multiple scattering and structural heterogeneity, so depolarization carries information that cannot be captured by retardance and diattenuation analysis alone.

For example, recent work has argued that retardance, diattenuation, and depolarization should be interpreted together in reflection geometry[129,130].

In practice, this direction suggests moving beyond treating Mueller-matrix-derived quantities as isolated scalar images and instead viewing them as a structured high-dimensional representation[65]. One possible route is to construct joint parameter spaces in which each pixel, region, or sample is described by its full polarimetric signature, and then use topology- or geometry-aware methods to study how these signatures are organized in space. Manifold learning and unsupervised clustering have already been applied to Mueller-matrix pathology data to reveal microstructural groupings that are not obvious in separate parameter maps[70]. Another route is to use data-driven fusion and AI to identify combinations of parameters that are most informative for tasks such as segmentation, tissue stratification, or defect detection[131].

5.2.2 Fusion of polarimetric and non-polarimetric information

A further direction for future work is to investigate how polarimetric information can be combined with broader forms of information for more advanced analysis and problem solving. This can be considered at two levels: (1) the combination of

polarimetric information with other optical information; and (2) its integration with broader non-optical information.

The first is to combine Mueller-matrix-derived parameters with other optical information. In many applications, polarimetric parameters provide only one part of the optical description of a sample. Other optical observables, including conventional images and measurements from modalities such as second-harmonic generation, optical coherence tomography, fluorescence, and hyperspectral imaging, may provide complementary information that is not captured by polarimetric parameters alone[4]. These different optical contrasts may reveal additional aspects of a sample, such as morphology[132–134], chemical composition[135], or biointerfaces[136,137]. The combination of these different types of information may therefore facilitate more accurate disease staging and diagnosis[138–140]. More generally, this direction is also relevant to material characterization and other measurement tasks, where polarimetric contrast and other optical imaging contrasts can provide complementary information about the same underlying structure[141,142].

The second is to integrate polarimetric information with broader non-optical information. In many practical problems, the useful complementary information is not another optical contrast, but an external variable. For example, medical AI

systems have combined imaging with clinical information for diagnosis[143], risk-assessment models have integrated imaging with genetic data[144], and materials informatics frameworks have fused microstructural images with processing conditions to learn richer representations of material systems[145]. These examples suggest that future polarimetric methods may also become more powerful when linked directly to the non-optical variables that matter for the application itself[146–148].

In terms of implementation, artificial intelligence provides a natural route for this type of information fusion, because they are well suited to learning complementary features from heterogeneous data sources[149]. In this setting, Mueller-matrix-derived parameters could be combined with non-polarimetric features, such as morphological, chemical, or molecular information, and used as joint inputs for learning-based models[62]. Depending on the task, early-fusion models may concatenate different parameter maps at the input level[150], whereas attention-based or transformer-based architectures can learn cross-modal relationships between different information sources[151]. These approaches could support tasks such as classification, segmentation, tissue stratification, or prediction[152–154].

An alternative route is to use topology-inspired methods. Related ideas have been proposed previously[70,155], and we believe that this direction has considerable potential for further development. In particular, different parameters may first be projected or mapped into a low-dimensional space to construct an object with topological meaning[156]. The resulting topological structure can then be analyzed to study different parameters within a unified framework[157].

References

1. Goldstein, D. H. *Polarized Light*. 3rd edn. (CRC Press, 2017).
2. Weiner, J. & Ho, P.-T. *Light-Matter Interaction: Fundamentals and Applications*. (John Wiley & Sons, 2008).
3. Gil, J. J. & Ossikovski, R. *Polarized Light and the Mueller Matrix Approach*. (CRC Press, New York, 2022). doi:10.1201/9780367815578.
4. He, C. *et al.* Polarisation optics for biomedical and clinical applications: a review. *Light Sci Appl* **10**, 194 (2021).
5. Tominaga, S. & Kimachi, A. Polarization imaging for material classification. *OE* **47**, 123201 (2008).
6. Forbes, A., de Oliveira, M. & Dennis, M. R. Structured light. *Nat. Photonics* **15**, 253–262 (2021).
7. Lu, S.-Y. & Chipman, R. A. Interpretation of Mueller matrices based on polar decomposition. *J. Opt. Soc. Am. A* **13**, 1106 (1996).
8. Ortega-Quijano, N. & Arce-Diego, J. L. Mueller matrix differential decomposition. *Opt. Lett.* **36**, 1942 (2011).
9. Ossikovski, R. Analysis of depolarizing Mueller matrices through a symmetric decomposition. *J. Opt. Soc. Am. A* **26**, 1109 (2009).
10. He, H. et al. A possible quantitative Mueller matrix transformation technique for anisotropic scattering media/Eine mögliche quantitative Müller-Matrix-

Transformations-Technik für anisotrope streuende Medien. *Photonics & Lasers in Medicine* 2, 129–137 (2013).

11. Guan, C., Zeng, N. & He, H. Review of polarization-based technology for biomedical applications. *J. Innov. Opt. Health Sci.* **18**, 2430002 (2025).
12. Hakobyan, V. & Brasselet, E. Q-Plates: From Optical Vortices to Optical Skyrmions. *Phys. Rev. Lett.* **134**, 083802 (2025).
13. Shi, Z. *et al.* Continuous angle-tunable birefringence with freeform metasurfaces for arbitrary polarization conversion. *Science Advances* **6**, eaba3367 (2020).
14. Mata-Cervera, N. *et al.* Tailoring propagation-invariant topology of optical skyrmions with dielectric metasurfaces. *Nanophotonics*. doi:10.1515/nanoph-2024-0736.
15. He, C. *et al.* Complex vectorial optics through gradient index lens cascades. *Nat Commun* **10**, 4264 (2019).
16. Shen, Y. *et al.* Topologically controlled multiskyrmions in photonic gradient-index lenses. *Phys. Rev. Applied* **21**, 024025 (2024).
17. Radwell, N., Hawley, R. D., Götte, J. B. & Franke-Arnold, S. Achromatic vector vortex beams from a glass cone. *Nat Commun* **7**, 10564 (2016).
18. He, C. et al. A universal optical modulator for synthetic topologically tuneable structured matter. *arXiv:2311.18148* (2023).

19. Hu, Q., He, C. & Booth, M. J. Arbitrary complex retarders using a sequence of spatial light modulators as the basis for adaptive polarisation compensation. *J. Opt.* **23**, 065602 (2021).

20. Deng, L. *et al.* Malus-metasurface-assisted polarization multiplexing. *Light Sci Appl* **9**, 101 (2020).

21. He, C., Shen, Y. & Forbes, A. Towards higher-dimensional structured light. *Light Sci Appl* **11**, 205 (2022).

22. Pedrotti, F. L., Pedrotti, L. M. & Pedrotti, L. S. *Introduction to Optics*. (Cambridge University Press, 2017).

23. Kliger, D. S., Lewis, J. W., Randall, C. E. & Azzam, R. M. A. *Polarized Light in Optics and Spectroscopy*. *Physics Today* **44**, 117–118 (1991).

24. Brosseau, C. *Fundamentals of Polarized Light: A Statistical Optics Approach*. (Wiley, New York, 1998).

25. Wolf, E. & Born, M. Principles of Optics: Electromagnetic Theory of Propagation, Interference and Diffraction of Light. in *Principles of Optics* (Elsevier Science & Technology, United Kingdom, 1980).

26. Novikova, T., Meglinski, I., Ramella-Roman, J. C. & Tuchin, V. V. Special Section Guest Editorial: Polarized Light for Biomedical Applications. *Journal of biomedical optics* **21**, 071001 (2016).

27. He, H. *et al.* Mueller Matrix Polarimetry—An Emerging New Tool for Characterizing the Microstructural Feature of Complex Biological Specimen. *J. Lightwave Technol.* **37**, 2534–2548 (2019).

28. Ghosh, N. Tissue polarimetry: concepts, challenges, applications, and outlook. *J. Biomed. Opt* **16**, 110801 (2011).

29. Tuchin, V. V. Polarized light interaction with tissues. *J. Biomed. Opt* **21**, 071114 (2016).

30. Ramella-Roman, J. C., Saytashev, I. & Piccini, M. A review of polarization-based imaging technologies for clinical and preclinical applications. *J. Opt.* **22**, 123001 (2020).

31. Chipman, R. A. *Polarized Light and Optical Systems*. (CRC Press, 2018). doi:10.1201/9781351129121.

32. Sridhar, S. & Da Silva, A. Enhanced contrast and depth resolution in polarization imaging using elliptically polarized light. *J. Biomed. Opt* **21**, 071107 (2016).

33. Qi, J., Ye, M., Singh, M., Clancy, N. T. & Elson, D. S. Narrow band 3 × 3 Mueller polarimetric endoscopy. *Biomed. Opt. Express* **4**, 2433 (2013).

34. Chang, J. *et al.* Division of focal plane polarimeter-based 3 × 4 Mueller matrix microscope: a potential tool for quick diagnosis of human carcinoma tissues. *Journal of biomedical optics* **21**, 056002 (2016).

35. Jacques, S. L., Ramella-Roman, J. C. & Lee, K. Imaging skin pathology with polarized light. *J. Biomed. Opt.* **7**, 329 (2002).

36. Jacques, S. L., Roman, J. R. & Lee, K. Imaging superficial tissues with polarized light. *Lasers Surg. Med.* **26**, 119–129 (2000).

37. Groner, W. *et al.* Orthogonal polarization spectral imaging: A new method for study of the microcirculation. *Nat Med* **5**, 1209–1212 (1999).

38. Bargo, P. R. & Kollias, N. Measurement of skin texture through polarization imaging: Measurement of skin texture through polarization imaging. *British Journal of Dermatology* **162**, 724–731 (2010).

39. Azzam, R. M. A. Photopolarimetric measurement of the Mueller matrix by Fourier analysis of a single detected signal. *Opt. Lett.* **2**, 148 (1978).

40. Goldstein, D. H. Mueller matrix dual-rotating retarder polarimeter. *Applied Optics* 31, 6676–6683 (1992).

41. Smith, M. H. Optimization of a dual-rotating-retarder Mueller matrix polarimeter. *Applied Optics* **41**, 2488–2493 (2002).

42. Laude-Boulesteix, B., Martino, A. D., Drévillon, B. & Schwartz, L. Mueller polarimetric imaging system with liquid crystals. *Appl. Opt.* **43**, 2824–2832 (2004).

43. Sornsin, E. A. & Chipman, R. A. Mueller matrix polarimetry of electro-optic PLZT spatial light modulators. in vol. 2873 196–201 (SPIE, 1996).

44. Alali, S., Gribble, A. & Vitkin, I. A. Rapid wide-field Mueller matrix polarimetry imaging based on four photoelastic modulators with no moving parts. *Optics letters* **41**, 1038–1041 (2016).

45. Dong, Y. *et al.* Deriving Polarimetry Feature Parameters to Characterize Microstructural Features in Histological Sections of Breast Tissues. *IEEE Trans. Biomed. Eng.* **68**, 881–892 (2021).

46. Ma, H., He, H. & Ramella-Roman, J. C. Mueller Matrix Microscopy. in *Polarized Light in Biomedical Imaging and Sensing: Clinical and Preclinical Applications* (eds Ramella-Roman, J. C. & Novikova, T.) 281–320 (Springer International Publishing, Cham, 2023). doi:10.1007/978-3-031-04741-1_11.

47. Oldenbourg, R. & Mei, G. New polarized light microscope with precision universal compensator. *Journal of microscopy (Oxford)* **180**, 140–147 (1995).

48. Oldenbourg, R. Polarized Light Microscopy: Principles and Practice. *Cold Spring Harb Protoc* **2013**, pdb.top078600 (2013).

49. Antonelli, M.-R. *et al.* Mueller matrix imaging of human colon tissue for cancer diagnostics: how Monte Carlo modeling can help in the interpretation of experimental data. *Opt. Express* **18**, 10200 (2010).

50. Pierangelo, A. *et al.* Ex-vivo characterization of human colon cancer by Mueller polarimetric imaging. *Opt. Express* **19**, 1582 (2011).

51. Chipman, R. A. Polarization Analysis Of Optical Systems. *OE* **28**, 90–99 (1989).

52. Manhas, S. *et al.* Mueller matrix approach for determination of optical rotation in chiral turbid media in backscattering geometry. *Opt. Express* **14**, 190 (2006).

53. Guo, Y. *et al.* A study on forward scattering Mueller matrix decomposition in anisotropic medium. *Opt. Express* **21**, 18361 (2013).

54. Ghosh, N., Wood, M. F. G. & Vitkin, I. A. Mueller matrix decomposition for extraction of individual polarization parameters from complex turbid media exhibiting multiple scattering, optical activity, and linear birefringence. *J. Biomed. Opt.* **13**, 044036 (2008).

55. Ossikovski, R. Differential matrix formalism for depolarizing anisotropic media. *Opt. Lett.* **36**, 2330 (2011).

56. Nan, Z., Xiaoyu, J., Qiang, G., Yonghong, H. & Hui, M. Linear polarization difference imaging and its potential applications. *Appl. Opt.* **48**, 6734 (2009).

57. Liao, R. *et al.* Rotating linear polarization imaging technique for anisotropic tissues. *J. Biomed. Opt.* **15**, 036014 (2010).

58. Gil, J. J. Invariant quantities of a Mueller matrix under rotation and retarder transformations. *J. Opt. Soc. Am. A* **33**, 52 (2016).

59. Li, P., Lv, D., He, H. & Ma, H. Separating azimuthal orientation dependence in polarization measurements of anisotropic media. *Opt. Express* **26**, 3791 (2018).

60. Li, P., Tariq, A., He, H. & Ma, H. Characteristic Mueller matrices for direct assessment of the breaking of symmetries. *Opt. Lett.* **45**, 706 (2020).

61. Li, G. et al. Marine oil slick detection using improved polarimetric feature parameters based on polarimetric synthetic aperture radar data. *Remote Sensing* 13, 1607 (2021).

62. Yang, K. *et al.* Data-driven polarimetric imaging: a review. *Opto-Electron Sci* **3**, 230042–44 (2024).

63. Dong, Y. *et al.* Quantitatively characterizing the microstructural features of breast ductal carcinoma tissues in different progression stages by Mueller matrix microscope. *Biomed. Opt. Express* **8**, 3643 (2017).

64. Liu, T. *et al.* Distinguishing structural features between Crohn's disease and gastrointestinal luminal tuberculosis using Mueller matrix derived parameters. *Journal of Biophotonics* **12**, e201900151 (2019).

65. Zhai, H. *et al.* Distinguishing tissue structures via polarization staining images based on different combinations of Mueller matrix polar decomposition parameters. *Optics and Lasers in Engineering* **152**, 106955 (2022).

66. Hou, A. *et al.* Polarimetry feature parameter deriving from Mueller matrix imaging and auto-diagnostic significance to distinguish HSIL and CSCC. *J. Innov. Opt. Health Sci.* **15**, 2142008 (2022).

67. Liu, X. *et al.* Discrimination and quantification of scar tissue by Mueller matrix imaging with machine learning. *J. Innov. Opt. Health Sci.* **16**, 2241003 (2023).

68. Dong, Y. *et al.* A Polarization-Imaging-Based Machine Learning Framework for Quantitative Pathological Diagnosis of Cervical Precancerous Lesions. *IEEE Trans. Med. Imaging* **40**, 3728–3738 (2021).

69. Ivanov, D. *et al.* Polarization-Based Histopathology Classification of Ex Vivo Colon Samples Supported by Machine Learning. *Front. Phys.* **9**, 814787 (2022).

70. Wan, J. *et al.* Unsupervised learning of pixel clustering in Mueller matrix images for mapping microstructural features in pathological tissues. *Commun Eng* **2**, 88 (2023).

71. Zhao, Y. *et al.* Detecting Giant Cell Tumor of Bone Lesions Using Mueller Matrix Polarization Microscopic Imaging and Multi-Parameters Fusion Network. *IEEE Sensors J.* **20**, 7208–7215 (2020).

72. Iannucci, L. E. et al. Optical imaging of dynamic collagen processes in health and disease. *Frontiers in Mechanical Engineering* 8, 855271 (2022).

73. Dong, Y., Liu, S., Shen, Y., He, H. & Ma, H. Probing variations of fibrous structures during the development of breast ductal carcinoma tissues via Mueller matrix imaging. *Biomedical optics express* **11**, 4960–4975 (2020).

74. Xia, L. et al. Mueller polarimetric microscopic images analysis based classification of breast cancer cells. *Optics Communications* 475, 126194 (2020).

75. Pierangelo, A. *et al.* Multispectral Mueller polarimetric imaging detecting residual cancer and cancer regression after neoadjuvant treatment for colorectal carcinomas. *J. Biomed. Opt* **18**, 046014 (2013).

76. Novikova, T. *et al.* The origins of polarimetric image contrast between healthy and cancerous human colon tissue. *Applied Physics Letters* **102**, 241103 (2013).

77. Ahmad, I. *et al.* Ex vivo characterization of normal and adenocarcinoma colon samples by Mueller matrix polarimetry. *J Biomed Opt* **20**, 56012 (2015).

78. Tumanova, K. *et al.* Mueller matrix polarization parameters correlate with local recurrence in patients with stage III colorectal cancer. *Sci Rep* **13**, 13424 (2023).

79. Pierangelo, A. *et al.* Polarimetric imaging of uterine cervix: a case study. *Opt. Express* **21**, 14120 (2013).

80. Rehbinder, J. *et al.* Ex vivo Mueller polarimetric imaging of the uterine cervix: A first statistical evaluation. *Journal of Biomedical Optics* **21**, 071113 (2016).

81. Shukla, P. & Pradhan, A. Mueller decomposition images for cervical tissue: Potential for discriminating normal and dysplastic states. *Opt. Express* **17**, 1600–1609 (2009).

82. Chue-Sang, J. et al. Use of combined polarization-sensitive optical coherence tomography and Mueller matrix imaging for the polarimetric characterization of excised biological tissue. *Journal of Biomedical Optics* 21, 071109 (2016).

83. Du, E. *et al.* Mueller matrix polarimetry for differentiating characteristic features of cancerous tissues. *J. Biomed. Opt* **19**, 076013 (2014).

84. Le, D. L., Nguyen, D. T., Le, T. H., Phan, Q.-H. & Pham, T.-T.-H. Characterization of healthy and cancerous human skin tissue utilizing Stokes–Mueller polarimetry technique. *Optics Communications* **480**, 126460 (2021).

85. Luu, T.-N., Phan, Q.-H., Le, T.-H. & Pham, T.-T.-H. Classification of human skin cancer using Stokes-Mueller decomposition method and artificial intelligence models. *Optik* **249**, 168239 (2022).

86. Wang, Y. *et al.* Mueller matrix microscope: a quantitative tool to facilitate detections and fibrosis scorings of liver cirrhosis and cancer tissues. *J. Biomed. Opt* **21**, 071112 (2016).

87. Dubreuil, M. *et al.* Mueller matrix polarimetry for improved liver fibrosis diagnosis. *Opt. Lett.* **37**, 1061 (2012).

88. Wang, W. *et al.* Roles of linear and circular polarization properties and effect of wavelength choice on differentiation between ex vivo normal and cancerous gastric samples. *J Biomed Opt* **19**, 046020 (2014).

89. Mi, C., Shao, C., He, H., He, C. & Ma, H. Evaluating Tissue Mechanical Properties Using Quantitative Mueller Matrix Polarimetry and Neural Network. *Applied Sciences* **12**, 9774 (2022).

90. Fricke, D. *et al.* Mueller Matrix Analysis of Collagen and Gelatin Containing Samples Towards More Objective Skin Tissue Diagnostics. *Polymers* **12**, 1400 (2020).

91. Qi, J. & Elson, D. S. A high definition Mueller polarimetric endoscope for tissue characterisation. *Sci Rep* **6**, 25953 (2016).

92. Ahmad, I., Gribble, A., Ikram, M., Pop, M. & Vitkin, A. Polarimetric assessment of healthy and radiofrequency ablated porcine myocardial tissue. *J Biophotonics* **9**, 750–759 (2016).

93. Sun, M. *et al.* Characterizing the microstructures of biological tissues using Mueller matrix and transformed polarization parameters. *Biomed. Opt. Express* **5**, 4223 (2014).

94. He, H. *et al.* Monitoring microstructural variations of fresh skeletal muscle tissues by Mueller matrix imaging. *Journal of Biophotonics* **10**, 664–673 (2017).

95. Ushenko, V. A. *et al.* 3D Mueller matrix mapping of layered distributions of depolarisation degree for analysis of prostate adenoma and carcinoma diffuse tissues. *Sci Rep* **11**, 5162 (2021).

96. Qi, J. *et al.* Surgical polarimetric endoscopy for the detection of laryngeal cancer. *Nat. Biomed. Eng* **7**, 971–985 (2023).

97. Vizet, J. *et al.* In vivo imaging of uterine cervix with a Mueller polarimetric colposcope. *Sci Rep* **7**, 2471 (2017).

98. Gonzalez, M. *et al.* Design and implementation of a portable colposcope Mueller matrix polarimeter. *J Biomed Opt* **25**, 116006 (2020).

99. Whitney, C. Pauli-algebraic operators in polarization optics. *Journal of the Optical Society of America* 61, 1207–1213 (1971).

100. Miller, S., Jiang, L. & Pau, S. Generalized elliptical retarder design and construction using nematic and cholesteric phase liquid crystal polymers. *Opt. Express* **30**, 16734 (2022).

101. Song, J., Guo, W., Zeng, N. & Ma, H. Polarization phase unwrapping by a dual-wavelength Mueller matrix imaging system. *Opt. Lett.* **48**, 2058 (2023).

102. Nguyen, T. L. *et al.* Quantitative Phase Imaging: Recent Advances and Expanding Potential in Biomedicine. *ACS Nano* **16**, 11516–11544 (2022).

103. Zhang, Y. *et al.* Skyrmions based on optical anisotropy for topological encoding. Preprint at https://doi.org/10.48550/arXiv.2508.16483 (2025).

104. Rosales-Guzmán, C., Ndagano, B. & Forbes, A. A review of complex vector light fields and their applications. *J. Opt.* **20**, 123001 (2018).

105. Milione, G., Nguyen, T. A., Leach, J., Nolan, D. A. & Alfano, R. R. Using the nonseparability of vector beams to encode information for optical communication. *Opt. Lett.* **40**, 4887–4890 (2015).

106. Zhu, Z. et al. Compensation-free high-dimensional free-space optical communication using turbulence-resilient vector beams. *Nature Communications* 12, 1666 (2021).

107. McMahon, P. L. The physics of optical computing. *Nat Rev Phys* **5**, 717–734 (2023).

108. Li, C., Zhang, X., Li, J., Fang, T. & Dong, X. The challenges of modern computing and new opportunities for optics. *PhotoniX* **2**, 20 (2021).

109. Mehmood, M. Q. *et al.* Visible-Frequency Metasurface for Structuring and Spatially Multiplexing Optical Vortices. *Advanced Materials* **28**, 2533–2539 (2016).

110. Chen, S., Liu, W., Li, Z., Cheng, H. & Tian, J. Metasurface-Empowered Optical Multiplexing and Multifunction. *Advanced Materials* **32**, 1805912 (2020).

111. Tang, D. *et al.* Flat multifunctional liquid crystal elements through multi-dimensional information multiplexing. *Opto-Electron Adv* **6**, 220063–9 (2023).

112. Skyrme, T. H. R. A unified field theory of mesons and baryons. *Nuclear Physics* 31, 556–569 (1962).

113. Shen, Y. *et al.* Optical skyrmions and other topological quasiparticles of light. *Nat. Photon.* **18**, 15–25 (2024).

114. Liu, C., Zhang, S., Maier, S. A. & Ren, H. Disorder-Induced Topological State Transition in the Optical Skyrmion Family. *Phys. Rev. Lett.* **129**, 267401 (2022).

115. Nape, I. *et al.* Revealing the invariance of vectorial structured light in complex media. *Nat. Photon.* **16**, 538–546 (2022).

116. Wang, A. A. *et al.* Topological protection of optical skyrmions through complex media. *Light Sci Appl* **13**, 314 (2024).

117. Wang, A. A. *et al.* Perturbation-resilient integer arithmetic using optical skyrmions. *Nat. Photon.* **19**, 1367–1375 (2025).

118. Meng, C., Thrane, P. C. V., Ding, F. & Bozhevolnyi, S. I. Full-range birefringence control with piezoelectric MEMS-based metasurfaces. *Nat Commun* **13**, 2071 (2022).

119. Wang, S. *et al.* Arbitrary polarization conversion dichroism metasurfaces for all-in-one full Poincaré sphere polarizers. *Light Sci Appl* **10**, 24 (2021).

120. Wang, S., Wen, S., Deng, Z.-L., Li, X. & Yang, Y. Metasurface-Based Solid Poincaré Sphere Polarizer. *Phys. Rev. Lett.* **130**, 123801 (2023).

121. Xiong, B. *et al.* Breaking the limitation of polarization multiplexing in optical metasurfaces with engineered noise. *Science* **379**, 294–299 (2023).

122. Balthasar Mueller, J. P., Rubin, N. A., Devlin, R. C., Groever, B. & Capasso, F. Metasurface Polarization Optics: Independent Phase Control of Arbitrary Orthogonal States of Polarization. *Phys. Rev. Lett.* **118**, 113901 (2017).

123. Bao, Y., Wen, L., Chen, Q., Qiu, C.-W. & Li, B. Toward the capacity limit of 2D planar Jones matrix with a single-layer metasurface. *Sci. Adv.* **7**, eabh0365 (2021).

124. Kleinman, D. A. Nonlinear Dielectric Polarization in Optical Media. *Phys. Rev.* **126**, 1977–1979 (1962).

125. Situ, G. & Zhang, J. Multiple-image encryption by wavelength multiplexing. *Opt. Lett.* **30**, 1306–1308 (2005).

126. Tomlinson, W. J. Wavelength multiplexing in multimode optical fibers. *Appl. Opt.* **16**, 2180–2194 (1977).

127. Bancelin, S. *et al.* Determination of collagen fiber orientation in histological slides using Mueller microscopy and validation by second harmonic generation imaging. *Opt. Express* **22**, 22561 (2014).

128. Yang, H. *et al.* Mueller matrix polarimetry for quantitative evaluation of the Achilles tendon injury recovery. *Front. Optoelectron.* **17**, 39 (2024).

129. Xie, Z. *et al.* Reciprocal polarization imaging of optical activity in reflection. *Opt. Lett.* **49**, 2349–2352 (2024).

130. Bonaventura, J. et al. Backscattering Mueller Matrix polarimetry on whole brain specimens shows promise for minimally invasive mapping of microstructural orientation features. *Frontiers in Photonics* 3, 1034739 (2022).

131. Pham, T.-T.-H. *et al.* Polarimetric imaging combining optical parameters for classification of mice non-melanoma skin cancer tissue using machine learning. *Heliyon* **9**, e22081 (2023).

132. Kim, K. et al. Optical diffraction tomography techniques for the study of cell pathophysiology. *Journal of Biomedical Photonics & Engineering* 2, 020201 (2016).

133. Fercher, A. F., Bartelt, H., Becker, H. & Wiltschko, E. Image formation by inversion of scattered field data: experiments and computational simulation. *Appl. Opt.* **18**, 2427–2439 (1979).

134. Wolf, E. Three-dimensional structure determination of semi-transparent objects from holographic data. *Optics Communications* **1**, 153–156 (1969).

135. Butler, H. J. *et al.* Using Raman spectroscopy to characterize biological materials. *Nat Protoc* **11**, 664–687 (2016).

136. Weigelin, B., Bakker, G.-J. & Friedl, P. Third harmonic generation microscopy of cells and tissue organization. *J Cell Sci* **129**, 245–255 (2016).

137. Débarre, D. *et al.* Imaging lipid bodies in cells and tissues using third-harmonic generation microscopy. *Nat Methods* **3**, 47–53 (2006).

138. Chue-Sang, J. *et al.* Use of Mueller matrix polarimetry and optical coherence tomography in the characterization of cervical collagen anisotropy. *J. Biomed. Opt.* **22**, 086010 (2017).

139. Liu, Y. *et al.* Complementary fluorescence-polarization microscopy using division-of-focal-plane polarization imaging sensor. *J. Biomed. Opt.* **17**, 116001 (2012).

140. Deng, L. *et al.* A Dual-Modality Imaging Method Based on Polarimetry and Second Harmonic Generation for Characterization and Evaluation of Skin Tissue Structures. *Int. J. Mol. Sci.* **24**, 4206 (2023).

141. Ge, B., Zhou, R., Takiguchi, Y., Yaqoob, Z. & So, P. T. C. Single-Shot Optical Anisotropy Imaging with Quantitative Polarization Interference Microscopy. *Laser & Photonics Reviews* **12**, 1800070 (2018).

142. Martínez-Prat, B., Arteaga, O., Sagués, F. & Ignés-Mullol, J. Multimodal fluorescence microscope with fast adaptive polarimetry. *HardwareX* **16**, e00480 (2023).

143. Ying, H. *et al.* A multicenter clinical AI system study for detection and diagnosis of focal liver lesions. *Nat Commun* **15**, 1131 (2024).

144. Huang, Y.-J., Chen, C. & Yang, H.-C. AI-enhanced integration of genetic and medical imaging data for risk assessment of Type 2 diabetes. *Nat Commun* **15**, 4230 (2024).

145. Wu, Y. *et al.* A versatile multimodal learning framework bridging multiscale knowledge for material design. *npj Comput Mater* **11**, 276 (2025).

146. Huang, S.-C., Pareek, A., Seyyedi, S., Banerjee, I. & Lungren, M. P. Fusion of medical imaging and electronic health records using deep learning: a systematic review and implementation guidelines. *npj Digit. Med.* **3**, 136 (2020).

147. Shi, R., Sun, J., Zhou, Z., Su, Q. & Shu, Y. Deep multimodal fusion of patho-radiomic and clinical data for enhanced survival prediction for colorectal cancer patients. *npj Digit. Med.* **9**, 86 (2025).

148. Jonnagaddala, J. *et al.* Multimodal analysis of whole slide images in colorectal cancer. *npj Digit. Med.* **8**, 719 (2025).

149. Stahlschmidt, S. R., Ulfenborg, B. & Synnergren, J. Multimodal deep learning for biomedical data fusion: a review. *Briefings in Bioinformatics* **23**, bbab569 (2022).

150. Gao, J., Li, P., Chen, Z. & Zhang, J. A Survey on Deep Learning for Multimodal Data Fusion. *Neural Computation* **32**, 829–864 (2020).

151. Xu, P., Zhu, X. & Clifton, D. A. Multimodal Learning With Transformers: A Survey. *IEEE Trans. Pattern Anal. Mach. Intell.* **45**, 12113–12132 (2023).

152. Teoh, J. R. *et al.* Advancing healthcare through multimodal data fusion: a comprehensive review of techniques and applications. *PeerJ Comput Sci* **10**, e2298 (2024).

153. Bi, Y., Abrol, A., Fu, Z. & Calhoun, V. D. A multimodal vision transformer for interpretable fusion of functional and structural neuroimaging data. *Hum Brain Mapp* **45**, e26783 (2024).

154. Xiao, L., Stephen, J. M., Wilson, T. W., Calhoun, V. D. & Wang, Y.-P. Alternating Diffusion Map Based Fusion of Multimodal Brain Connectivity Networks for IQ Prediction. *IEEE Trans Biomed Eng* **66**, 2140–2151 (2019).

155. Levenson, R. M. *et al.* Advancing Precision Medicine: Algebraic Topology and Differential Geometry in Radiology and Computational Pathology. *Lab Invest* **104**, 102060 (2024).

156. Singh, G., Mémoli, F. & Carlsson, G. E. Topological methods for the analysis of high dimensional data sets and 3D object recognition. *Eurographics Symposium on Point-Based Graphics* 91–100 (2007).

157. Silva, V. de & Vejdemo-Johansson, M. Persistent Cohomology and Circular Coordinates. in *Proceedings of the twenty-fifth annual symposium on Computational geometry* 227–236 (2009). doi:10.1145/1542362.1542406.